A computational framework for the analysis of linear piezoelectric beams using hp-FEM

Roman Poya, Antonio J. Gil, Paul D. Ledger

Zienkiewicz Centre for Computational Engineering, College of Engineering, Swansea University, Singleton Park, SA2 8PP, United Kingdom

Abstract

In this paper, a new computational framework is introduced for the analysis of three dimensional linear piezoelectric beams using hp-finite elements. Unlike existing publications, the framework is very general and suitable for static, modal and dynamic scenarios; it is not restricted to either actuation or energy harvesting applications and, moreover, it can cope with any anisotropy or electric polarisation orientation. Derived from first principles, namely the fundamental equations of continuum piezoelectricity, a new set of beam balance equations is presented based on a Taylor series expansion for the displacement and electric potential across the cross section of the beam. The coupled nature of the piezoelectric phenomenon at a beam level arises via a series of mechanical (and electrical counterparts) stress and strain cross sectional area resultants. To benchmark the numerical algorithm, and in order to aid prospective researchers, a new closed-form solution is presented for the case of cantilever type systems subjected to end tip mechanical/electrical loads. To the best of the authors' knowledge, the analytical solution for this prototypical example has not been previously presented. Finally, some numerical aspects of the hp-discretisation are investigated including the exponential convergence of the hp-refinements and the consideration of linear or quadratic electric potential expansions across the cross section of the beam.

Keywords: Piezoelectric beam, piezoelectricity, hp-finite elements, benchmarking, energy harvesting, actuation

1. Introduction

Piezoelectric materials are exploited mainly for two major applications: actuation and sensing/energy harvesting. Energy harvesting implies induced electric polarisation as a result of mechanical straining (direct effect), whereas actuation implies induced mechanical straining as a result of electric polarisation (reverse effect) [1]. Certainly, these two phenomena can be viewed as unrelated, where different theoretical and numerical approaches can be employed. For instance, models of piezoelectric actuators have been devised with only mechanical degrees of freedom [2, 3, 4] and models of energy harvesters have been developed with more emphasis on electrical unknowns or, essentially, the final power output [1, 5, 6].

In this paper, by starting from the fundamental equations of continuum piezoelectricity, a unified static and dynamic computational framework is presented for three-dimensional piezoelectric beams, focussing on small strain theory (small electric fields) and straight beam axis. Mathematically, many of the well-established piezoelectric actuator models in the literature [4, 2, 3, 7] can be regarded as special cases which sit within this unified formulation. The merit of approaching the problem in this fashion is that the strengths and limitations of the formulation can be easily identified for both actuators and energy harvesters applications, without placing a distinction upon one or the other.

Some approaches can be found in the literature in the form of simplified single degree of freedom systems or two-dimensional beams, which are often referred to as lumped parameter and distributed parameter models, respectively [1, 6, 8, 9, 10, 11]. In the lumped parameter model, the piezoelectric device is constructed via a mass-spring-damper system coupled with a capacitor and a resistor [12, 6, 13]. However, this simplified model lacks some important aspects of the coupled physical system, such as the consideration of high dynamic modes, an accurate distribution of the strain field and the effects of the former two into the overall electrical response [1]. The distributed parameter model, on the other hand, is based upon Euler-Bernoulli beam theory, neglecting rotation of the cross section with respect to the beam axis, possible shear deformation and rotational inertia [14, 5].

One of the main simplifying assumptions in almost all of these approaches is that of vanishing electric field in certain directions, depending on the orientation of polarisation [6, 3, 8, 9, 4, 10]. In piezoelectric beam literature, these are normally referred to as different modes of coupling and are denoted

by d_{ij}, $i, j = 1 \ldots 6$ where d is the piezoelectric coupling parameter and the subscripts i and j indicate the poling direction and applied stress direction (in Voigt notation), respectively [15], with $i = 3$ or $j = 3$ representing the axial direction. In this setting, the two most common coupling mechanisms [2, 3, 4] are the d_{31} mode (shear actuation), which implies a coupling between the transverse electric field and axial strain and the d_{33} mode (extension actuation), which stands for coupling between the axial electric field and axial strain [6], with other coupling field mechanisms normally assumed to be zero.

On the mathematical modelling front, Benjeddou [3] attempts to build a unified two-dimensional (planar) beam finite element model for extension and shear actuation mechanisms. Tabesh [13] attempts to solve the problem of energy harvesting piezoelectric planar beams by employing Euler-Bernoulli theory with quadratic electric potential distribution across the height of the beam. As stated in [13, 16], a linear electric potential assumption is not sufficient to describe the electrostatics of the model as it violates Gauss's law, although many conventional models in the literature rely on this assumption [4, 6, 17].

Available literature on the numerical modelling of three-dimensional piezoelectric beams is scarce, specifically in the context of energy harvesting. Whilst a two-dimensional approach is sufficient for bending dominated energy harvesters, it is not satisfactory for capturing accurately piezoelectric (anisotropic) behaviour. Indeed, energy harvesters undergoing coupled bending-torsion [10] require a three-dimensional description. Moreover, there are actuators specifically designed to function in torsional modes such as helical springs [18, 19], for which two-dimensional descriptions cannot be used.

Wagner and co-workers [19, 20, 21] introduce a sophisticated three-dimensional beam finite element model with linear and nonlinear strain measures, including hysteresis, using a six field variational formulation and assuming a quadratic electric potential distribution across the cross sectional area. The work is restricted to static analysis only and requires a preprocessing stage to compute the warping patterns by solving a two-dimensional boundary value problem, using a separate finite element discretisation.

Another three-dimensional finite element formulation for piezoelectric beams is reported by Touratier [22]. Touratier's formulation is based on higher order shear deformation theory and trigonometric expansion of the displacement field, where for C^1 continuity, a mixture of Hermite, quadratic and linear shape functions are utilised. A similar technique is also followed to incorporate the warping functions in the beam model. As a result, each beam

finite element has three nodes along the length with 27 electrical degrees of freedom and 21 mechanical degrees of freedom. The work is restricted to static analysis and hence cannot be used for energy harvesting. Along the same lines, Koutsawa [23] attempts to solve the problem of static piezoelectric beams by using higher order displacement theories for beams.

This paper aims to present a simple three-dimensional finite element computational framework for linear piezoelectric beams, derived from first principles, in order to bridge the gap between existing simplified lumped or distributed parameter models [1, 6, 8, 9, 10, 12, 13] and the most sophisticated nonlinear warping beam models [19, 20, 21, 22, 23]. In the process, interesting new physical magnitudes, such as the coupled shear or the coupled bending/torsional moment introduced as a result of an electric displacement, will naturally arise. A similar approach to the one presented in this paper is pursued by Kushnir [7], with the difference that Kushnir's formulation is on ferro-electricity and is restricted to two-dimensions and static analysis only.

The linearised kinematics of the beam follows the first order shear deformation theory of Timoshenko and the electric potential field is assumed to vary quadratically across the height and thickness of the beam section. The electric potential distribution is expanded in terms of the electric potential, its gradient and its Hessian, all being evaluated at the centre of mass of the cross section (i.e. second order Taylor expansion about the centre of mass). Following [24, 25], the postulated beam kinematics and electric field distribution are embedded into the variational form of the continuum piezoelectric problem. Standard beam integration across the cross sectional area can then be carried out to yield a set of partial differential equations (e.g. time and beam axis as independent variables) that are expressed in terms of stress and electric displacement beam resultants (e.g. shear force and moments). Crucially, a consistent use of anisotropic elastic, piezoelectric and dielectric constitutive tensors, enables strains and electric fields to be coupled in all three spatial directions, with no preference to a specific orientation.

From the spatial discretisation standpoint, locking effects are eliminated through the use of higher order as well as hierarchical basis functions [26, 27, 28]. The resulting *hp*-finite element discretisation has eleven degrees of freedom per node [1] in three-dimensions and five degrees of freedom per node

---

[1]Strictly speaking, for hierarchical basis functions, the degrees of freedom are not associated with nodes but, instead, with polynomial coefficients.

in two-dimensions, namely displacements, rotations, electric potential, gradient of electric potential and Hessian of electric potential. The computational framework is valid for static, modal and dynamic scenarios, the latter being of interest for energy harvesting. The set of resulting partial differential equations have also been solved analytically with the purpose of obtaining closed-form solutions, which, to the best of the authors' knowledge, are presented here for the first time and are suitable for the benchmarking of the finite element computational framework.

The structure of the paper is as follows. Section 2 describes the balance equations of electromechanics and in Section 3 we introduce the kinematics and electrostatics of three-dimensional piezoelectric beams. Section 4 describes the variational formulation from which the mechanical and electrical cross sectional balance equations are obtained in Section 5. Analytical solutions for planar piezoelectric beams are presented in Section 6 and the hp-finite element discretisation of the variational formulation is presented in Section 7. Finally, in Section 8 a series of numerical simulations ranging from static to modal and dynamic analyses are reported.

2. Balance equations of electromechanics

Let $\Omega \subset \mathbb{R}^3$ be a bounded contractible domain occupied by a continuum during the time interval $[0, \mathrm{T}]$ and Γ be its boundary, equipped with a unit outward normal $\boldsymbol{n}$, as shown in Figure 1. In this case, the static Faraday and Gauss laws can be summarised as follows

$$\mathrm{curl}\boldsymbol{E} = \boldsymbol{0} \quad \text{and} \quad \mathrm{div}\boldsymbol{D} + \rho^e = 0 \quad \text{in } \Omega \times [0, \mathrm{T}], \tag{1}$$

where $\boldsymbol{E}$ denotes the electric field intensity vector, $\boldsymbol{D}$ is the electric displacement vector and ρ^e is the volume charge density. As Ω is a contractible domain, the electric field vector $\boldsymbol{E}$ can be reformulated as $\boldsymbol{E} = -\boldsymbol{\nabla}\phi$, where ϕ is a scalar potential field. Dirichlet and Neumann boundary conditions can then be introduced as

$$\phi = \bar{\psi} \quad \text{on} \quad \Gamma^{\psi} \times [0, \mathrm{T}], \tag{2a}$$

$$\boldsymbol{D} \cdot \boldsymbol{n} = \omega \quad \text{on} \quad \Gamma^D \times [0, \mathrm{T}]. \tag{2b}$$

where $\Gamma = \Gamma^D \cup \Gamma^{\psi}$ and $\Gamma^D \cap \Gamma^{\psi} = \emptyset$. In the context of small deformations, the motion of the continuum can be defined by a displacement field $\boldsymbol{u} : \Omega \times [0, \mathrm{T}] \to \mathbb{R}^3$, such that $(\boldsymbol{x}, t) \mapsto \boldsymbol{u}(\boldsymbol{x}, t)$, where $\boldsymbol{x} \in \Omega$ represents a

material point and $t \in [0, \text{T}]$ the time. The conservation of linear momentum equation is defined as

$$\text{div}\boldsymbol{\sigma} + \rho\boldsymbol{b} = \rho\ddot{\boldsymbol{u}} \quad \text{in } \Omega \times [0, \text{T}], \tag{3}$$

where ρ is the density of the continuum, $\boldsymbol{\sigma}$ is the symmetric (conservation of angular momentum) Cauchy stress tensor, $\boldsymbol{b}$ is a body force per unit of mass and a superimposed dot (double dot) indicates partial (double) differentiation with respect to time (e.g. $\dot{} := \frac{\partial}{\partial t}$ and $\ddot{} := \frac{\partial^2}{\partial t^2}$). Dirichlet, Neumann and initial conditions can be introduced as

$$\boldsymbol{u} = \bar{\boldsymbol{u}} \quad \text{on} \quad \Gamma^u \times [0, \text{T}], \tag{4a}$$

$$\boldsymbol{\sigma}\boldsymbol{n} = \boldsymbol{t} \quad \text{on} \quad \Gamma^\sigma \times [0, \text{T}], \tag{4b}$$

$$\boldsymbol{u} = \boldsymbol{u}_0 \quad \text{in} \quad \bar{\Omega} \times 0, \tag{4c}$$

$$\dot{\boldsymbol{u}} = \dot{\boldsymbol{u}}_0 \quad \text{in} \quad \bar{\Omega} \times 0, \tag{4d}$$

where $\Gamma = \Gamma^\sigma \cup \Gamma^u$ and $\Gamma^\sigma \cap \Gamma^u = \emptyset$. The coupled electro-mechanical initial boundary value problem, defined by equations (1) to (4), must be complemented with two closure equations related to the electro-mechanical nature of the continuum. For a conservative material, the closure equations can be derived from the enthalpy density of the system Ψ defined in terms of the electric field vector $\boldsymbol{E}$ and the small strain tensor $\boldsymbol{\varepsilon}$ as follows

$$\boldsymbol{\sigma}(\boldsymbol{\varepsilon}, \boldsymbol{E}) := \frac{\partial \Psi(\boldsymbol{\varepsilon}, \boldsymbol{E})}{\partial \boldsymbol{\varepsilon}} \quad \text{and} \quad \boldsymbol{D}(\boldsymbol{\varepsilon}, \boldsymbol{E}) := -\frac{\partial \Psi(\boldsymbol{\varepsilon}, \boldsymbol{E})}{\partial \boldsymbol{E}}, \quad \boldsymbol{\varepsilon} := \frac{1}{2}\left(\nabla\boldsymbol{u} + \nabla\boldsymbol{u}^T\right), \tag{5}$$

expressing the total Cauchy stress tensor $\boldsymbol{\sigma}$ and the electric displacement vector $\boldsymbol{D}$ in terms of the electric field $\boldsymbol{E}$ and the small strain tensor $\boldsymbol{\varepsilon}$. A variety of electro-mechanical constitutive models are available in the literature defined in terms of different enthalpy expressions [28, 29]. In the case of linear piezoelectricity, $\boldsymbol{\sigma}$ and $\boldsymbol{D}$ obtained this way render algebraic summations of mechanical $(\cdot)^m$ and electrical $(\cdot)^e$ components. [2]

The electric displacement $\boldsymbol{D}$ can be expanded as

$$\boldsymbol{D} = \boldsymbol{D}^m + \boldsymbol{D}^e; \quad \boldsymbol{D}^m := \boldsymbol{\mathcal{P}} : \boldsymbol{\varepsilon}, \quad \boldsymbol{D}^e := \boldsymbol{\epsilon}\boldsymbol{E}, \tag{6}$$

---

[2]Throughout the paper, the symbol $(\cdot)$ is used to indicate the scalar product or contraction of a single index $\boldsymbol{a} \cdot \boldsymbol{b} = a_i b_i$; the symbol $(:)$ is used to indicate double contraction of two indices $\boldsymbol{A} : \boldsymbol{B} = A_{ij}B_{ij}$; the symbol $(\times)$ is used to indicate the cross product $[\boldsymbol{a} \times \boldsymbol{b}]_i = \varepsilon_{ijk}a_j b_k$ via the third order permutation tensor ε_{ijk} and the symbol $(\otimes)$ is used to indicate the outer or dyadic product $[\boldsymbol{a} \otimes \boldsymbol{b}]_{ij} = a_i b_j$.

where $\boldsymbol{\epsilon}$ is the symmetric second order dielectric permittivity tensor and $\boldsymbol{\mathcal{P}}$ is the third order piezoelectric tensor verifying $[\boldsymbol{\mathcal{P}}]_{ijk} = [\boldsymbol{\mathcal{P}}]_{ikj}$. Analogously, the total Cauchy stress tensor $\boldsymbol{\sigma}$ can be decomposed additively as

$$\boldsymbol{\sigma} = \boldsymbol{\sigma}^m + \boldsymbol{\sigma}^e; \quad \boldsymbol{\sigma}^m := \boldsymbol{\mathcal{C}} : \boldsymbol{\varepsilon}, \quad \boldsymbol{\sigma}^e := -\boldsymbol{E} \cdot \boldsymbol{\mathcal{P}}. \tag{7}$$

Piezoelectric materials exhibit anisotropic behaviour and, hence, $\boldsymbol{\mathcal{C}}$ is the general fourth order anisotropic elasticity tensor satisfying $[\boldsymbol{\mathcal{C}}]_{ijkl} = [\boldsymbol{\mathcal{C}}]_{jikl} = [\boldsymbol{\mathcal{C}}]_{ijlk} = [\boldsymbol{\mathcal{C}}]_{klij}$. It is important to emphasise that the conservation of angular momentum requires the symmetry of $\boldsymbol{\sigma}$ but not of its individual components $\boldsymbol{\sigma}^m$ and $\boldsymbol{\sigma}^e$. Finally, the initial boundary value problem of the coupled problem is defined by equations (1)-(4), (6)-(7).
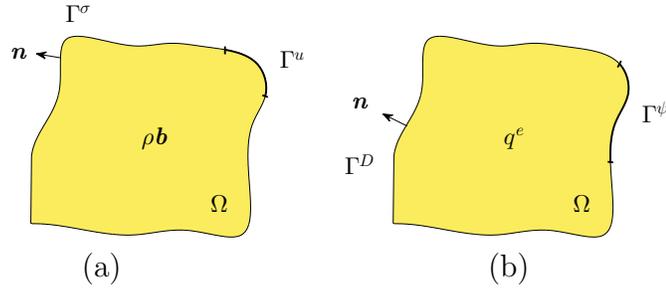
Figure 1: Decomposition of (a) Mechanical Boundary $\Gamma = \Gamma^\sigma \cup \Gamma^u$ and $\Gamma^\sigma \cap \Gamma^u = \emptyset$ and (b) Electrical Boundary $\Gamma = \Gamma^D \cup \Gamma^\psi$ and $\Gamma^D \cap \Gamma^\psi = \emptyset$

## 3. Kinematics and electrostatics of three-dimensional piezoelectric beams

3.1. Kinematics

Let us consider the motion of a beam $\Omega \subset \mathbb{R}^3$ as shown in Figure 2 [30]. The beam in the undeformed configuration has a straight axis of length l and is completely characterised with an orthonormal reference triad $\{\boldsymbol{e}_1, \boldsymbol{e}_2, \boldsymbol{e}_3\}$, where $\boldsymbol{e}_3$ is parallel to the beam axis and $\{\boldsymbol{e}_\alpha\}(\alpha = 1, 2)$ lie in the plane which defines the cross sectional area A (with boundary ∂A) of the beam $\Omega = A \times l$[3]. Assuming for simplicity that this reference frame (placed at

---

[3]Throughout the remainder of the paper, any Greek indices will be assumed to vary in the integer interval [1,2] and Latin indices to vary in the integer interval [1,2,3].

$[0, 0, x_3]^T$) coincides with the global one (placed at $[0, 0, 0]^T$), as shown in Figure 2, the beam current configuration $\boldsymbol{x} = [x_1, x_2, x_3]^T$ can be defined through a mapping $\boldsymbol{\varphi} : \Omega \times [0, T] \to \mathbb{R}^3$ as
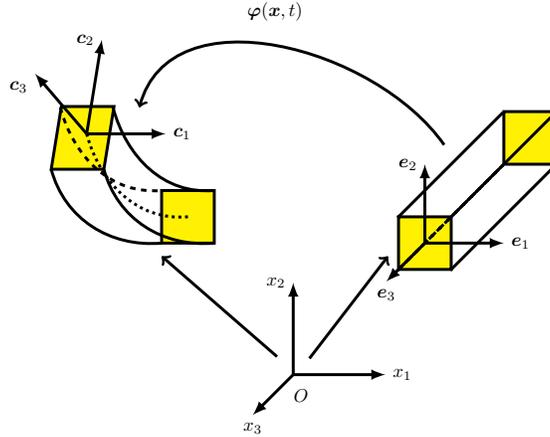
Figure 2: Motion of Beam in $\mathbb{R}^3$. The initial orthonormal triad $\{\boldsymbol{e}_1, \boldsymbol{e}_2, \boldsymbol{e}_3\}$ transforms to the orthonormal triad $\{\boldsymbol{c}_1, \boldsymbol{c}_2, \boldsymbol{c}_3\}$.

$$(\boldsymbol{x}, t) \mapsto \boldsymbol{\varphi}(\boldsymbol{x}, t) = x_3 \boldsymbol{e}_3 + \boldsymbol{w}(x_3, t) + \boldsymbol{\Lambda}(x_3, t) \boldsymbol{p}(x_1, x_2), \qquad (8)$$

where $\boldsymbol{p}(x_1, x_2) := x_\alpha \boldsymbol{e}_\alpha$ is the position vector of a material point within the cross section A with respect to the origin of the triad $\{\boldsymbol{e}_1, \boldsymbol{e}_2, \boldsymbol{e}_3\}$[4], $\boldsymbol{w}(x_3, t)$ is the displacement vector of the reference triad origin and $\boldsymbol{\Lambda}(x_3, t)$ is an orthogonal tensor evaluated at the triad origin and representing the transformation of the reference orthonormal triad $\{\boldsymbol{e}_1, \boldsymbol{e}_2, \boldsymbol{e}_3\}$ to a new orthonormal triad $\{\boldsymbol{c}_1, \boldsymbol{c}_2, \boldsymbol{c}_3\}$ according to $\boldsymbol{c}_i = \boldsymbol{\Lambda} \boldsymbol{e}_i$. It is well known, this rotation tensor $\boldsymbol{\Lambda}$ can be obtained in terms of the exponential mapping of a skew symmetric second order tensor $\hat{\boldsymbol{\theta}}$ and can be expanded in the form

$$\boldsymbol{\Lambda} = \exp(\hat{\boldsymbol{\theta}}) = \boldsymbol{I} + \hat{\boldsymbol{\theta}} + \frac{1}{2!}\hat{\boldsymbol{\theta}}^2 + \frac{1}{3!}\hat{\boldsymbol{\theta}}^3 + \dots \text{ as } \|\hat{\boldsymbol{\theta}}\| \to 0 \qquad (9)$$

where $\| \cdot \|$ denotes the standard Euclidean vector norm and $\hat{\boldsymbol{\theta}}$ is the skew-symmetric tensor associated with $\boldsymbol{\theta}$ [24]. Note that for any arbitrary vector

---

[4]Note that unless otherwise stated, Einstein's summation convention will be assumed.

$\boldsymbol{v} \in \mathbb{R}^3$ the following identity is fulfilled[5]

$$\boldsymbol{\theta} \times \boldsymbol{v} = \hat{\boldsymbol{\theta}}\boldsymbol{v}. \tag{10}$$

In the case of small rotations and neglecting high order terms, the rotation tensor can be approximated as $\boldsymbol{\Lambda} \simeq \boldsymbol{I} + \hat{\boldsymbol{\theta}}$ yielding a final displacement field $\boldsymbol{u} : \Omega \times [0,T] \to \mathbb{R}^3$ (refer to equation (8)) defined as

$$(\boldsymbol{x}, t) \mapsto \boldsymbol{u}(\boldsymbol{x}, t) = \boldsymbol{w}(x_3, t) + \boldsymbol{\theta}(x_3, t) \times \boldsymbol{p}(x_1, x_2), \tag{11}$$

where the vectors $\boldsymbol{w} = w_i \boldsymbol{e}_i$ and $\boldsymbol{\theta} = \theta_i \boldsymbol{e}_i$ are collectively called the generalised beam displacements. Expression (11) represents a time dependent affine mapping for any material point contained within the cross sectional area A of the beam. Noticing that $\boldsymbol{\nabla}\boldsymbol{u} = \frac{\partial \boldsymbol{u}}{\partial x_i} \otimes \boldsymbol{e}_i$ and $\frac{\partial \boldsymbol{p}}{\partial x_\alpha} = \boldsymbol{e}_\alpha$, the small strain tensor $\boldsymbol{\varepsilon}$ can be rewritten as

$$\boldsymbol{\varepsilon} = \frac{1}{2}\left[(\boldsymbol{\epsilon}^m + \boldsymbol{\kappa}^m \times \boldsymbol{p}) \otimes \boldsymbol{e}_3 + \boldsymbol{e}_3 \otimes (\boldsymbol{\epsilon}^m + \boldsymbol{\kappa}^m \times \boldsymbol{p})\right], \tag{12}$$

where

$$\boldsymbol{\epsilon}^m := \frac{\partial \boldsymbol{w}}{\partial x_3} + \boldsymbol{e}_3 \times \boldsymbol{\theta}, \qquad \boldsymbol{\kappa}^m := \frac{\partial \boldsymbol{\theta}}{\partial x_3}, \tag{13}$$

are called the strain resultants of the linear beam model, which characterise translational deformation and rotational deformation, respectively.

3.2. Electrical Mapping

Similar to the previous section, we postulate a Taylor series expansion for the electric potential $\phi : \Omega \times [0,T] \to \mathbb{R}$ in the form

$$\begin{aligned}(\boldsymbol{x}, t) \mapsto \phi(\boldsymbol{x}) = &\phi\,|_{(0,0,x_3,t)} + \boldsymbol{p}(x_1, x_2) \cdot \boldsymbol{\nabla}\phi\,|_{(0,0,x_3,t)} + \\ &\frac{1}{2}\boldsymbol{p}(x_1, x_2) \cdot \boldsymbol{H}_\phi\,|_{(0,0,x_3,t)}\,\boldsymbol{p}(x_1, x_2) + \dots \text{ as } \|\boldsymbol{p}(x_1, x_2)\| \to 0\end{aligned} \tag{14}$$

in terms of the time dependent electric potential ϕ, its vector gradient $\boldsymbol{\nabla}\phi$ and its second order tensor Hessian $\boldsymbol{H}_\phi$ defined at the reference triad origin

---

[5]In general, given any vector $\boldsymbol{a} \in \mathbb{R}^3$, the corresponding skew symmetric second order tensor $\hat{\boldsymbol{a}}$ may be defined according to equation (??).

$[0, 0, x_3]^T$. It is possible to neglect high order terms $\mathcal{O}(\|\boldsymbol{p}(x_1, x_2)\|^3)$ by assuming that the spatial variation of the electric potential in the cross section of the beam is sufficiently well defined via $\boldsymbol{\nabla}\phi$ and $\boldsymbol{H}_\phi$, in line with references [19, 7]. Notice that any lower order electric potential interpolation across the section of the beam would yield a non-varying electric field vector $\boldsymbol{E}$ across A. With this assumption in place, we can introduce an approximate electric potential field $\psi : \Omega \times [0, T] \to \mathbb{R}$ defined as

$$(\boldsymbol{x}, t) \mapsto \psi(\boldsymbol{x}, t) := \phi(x_3, t) + \boldsymbol{p}(x_1, x_2) \cdot \boldsymbol{\beta}(x_3, t) + \frac{1}{2}\boldsymbol{p}(x_1, x_2) \cdot \boldsymbol{\gamma}(x_3, t) \, \boldsymbol{p}(x_1, x_2),$$
(15)

where ψ represents a parabolic expansion across the cross sectional area A of the beam, completely defined in terms of ϕ, $\boldsymbol{\beta}$ and $\boldsymbol{\gamma}$, namely scalar, vector and symmetric second order tensor beam axis-varying functions. It is important to remark that the only approximation for the distribution of the electric potential is established across the section of the beam (see Figure 3). The variation along the beam axis remains without any approximation.

The electric field vector $\boldsymbol{E}$ can now be obtained by computing the gradient of the newly introduced electric potential ψ as $\boldsymbol{E} := -\boldsymbol{\nabla}\psi$ yielding (refer to equation (15)), after some algebraic manipulation

$$\boldsymbol{E} = -\boldsymbol{\epsilon}^e - (\boldsymbol{e}_3 \otimes \boldsymbol{p})\boldsymbol{\kappa}^e - \boldsymbol{\mathcal{V}} : \boldsymbol{\varsigma}^e - \boldsymbol{\mathcal{W}} : \boldsymbol{\gamma},$$
(16)

where

$$\boldsymbol{\epsilon}^e := \frac{\partial\phi}{\partial x_3}\boldsymbol{e}_3 + \boldsymbol{\beta}, \qquad \boldsymbol{\kappa}^e := \frac{\partial\boldsymbol{\beta}}{\partial x_3}, \qquad \boldsymbol{\varsigma}^e := \frac{\partial\boldsymbol{\gamma}}{\partial x_3},$$
(17)

with the third order tensors $\boldsymbol{\mathcal{V}}$ and $\boldsymbol{\mathcal{W}}$ defined by

$$\boldsymbol{\mathcal{V}} := \boldsymbol{e}_3 \otimes \frac{1}{2}\left(\boldsymbol{p} \otimes \boldsymbol{p}\right), \qquad \boldsymbol{\mathcal{W}} := \boldsymbol{e}_\alpha \otimes \frac{1}{2}\left(\boldsymbol{p} \otimes \boldsymbol{e}_\alpha + \boldsymbol{e}_\alpha \otimes \boldsymbol{p}\right).$$
(18)

Considering equation (16), it is interesting to notice the similarities with the definition of the small strain tensor $\boldsymbol{\varepsilon}$ (12). Notice how the first two terms on the right hand side of equation (16) stem from the linear contribution in (15) (as in formula (12)) whereas the last two terms stem from the quadratic contribution in (15).

10
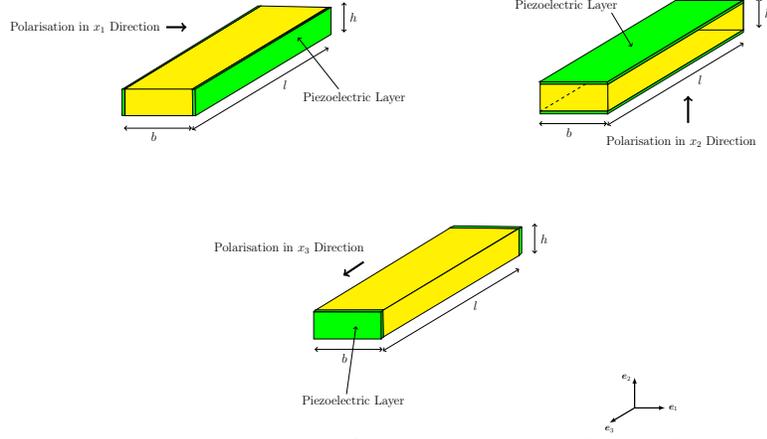
Figure 3: Electrostatics of a three-dimensional piezoelectric beam

The new initial boundary value problem, adapted to a three-dimensional beam problem, is then defined by equations (1-7) and (11,15), which combine the governing equations of both elastodynamics and electrostatics, initial and boundary conditions, the coupling electro-mechanical equations for $\boldsymbol{\sigma}$ and $\boldsymbol{D}$, the beam kinematics assumption $\boldsymbol{u}$ and the electric potential spatial distribution ψ. Notice that the initial and boundary conditions must be compatible with the assumptions for the beam kinematics and the electric potential spatial distribution. The variables of the resulting electromechanical beam model in a general three-dimensional beam problem are $\{\boldsymbol{w}, \boldsymbol{\theta}, \phi, \boldsymbol{\beta}, \boldsymbol{\gamma}\}$ defined in $l \times [0, T]$.

4. Variational formulation

In order to establish the variational formulation of the problem, the following spaces of admissible trial functions $\boldsymbol{u}$ and ψ are considered:

$$\boldsymbol{\mathcal{V}}_{\bar{\boldsymbol{u}}}^{\boldsymbol{u}} := \{\boldsymbol{u} \mid \boldsymbol{u} := \boldsymbol{w} + \boldsymbol{\theta} \times \boldsymbol{p}, \quad \boldsymbol{u} = \bar{\boldsymbol{u}} \text{ on } \Gamma^u \times [0, T]\}, \qquad (19)$$

$$\mathcal{V}_{\bar{\psi}}^{\psi} := \left\{\psi \mid \psi := \phi + \boldsymbol{p} \cdot \boldsymbol{\beta} + \frac{1}{2}\boldsymbol{p} \cdot \boldsymbol{\gamma} \cdot \boldsymbol{p}, \quad \psi = \bar{\psi} \text{ on } \Gamma^\psi \times [0, T]\right\}, \quad (20)$$

with the component functions $\{(\boldsymbol{w} \cdot \boldsymbol{e}_i), (\boldsymbol{\theta} \cdot \boldsymbol{e}_i), \phi, (\boldsymbol{\beta} \cdot \boldsymbol{e}_\alpha), (\boldsymbol{e}_\alpha \cdot \boldsymbol{\gamma} \boldsymbol{e}_\beta)\} \in H^1(\Omega)$. Following a standard variational methodology [28, 29], the variational form (virtual work) of the initial boundary value problem is given as:

11

Find $(\boldsymbol{u}, \psi) \in \boldsymbol{\mathcal{V}_{\bar{\boldsymbol{u}}}^{\boldsymbol{u}}} \times \mathcal{V}_{\bar{\psi}}^{\psi}$ such that

$$\delta W(\boldsymbol{u}, \psi; \delta\boldsymbol{u}, \delta\psi) := \delta W_{iner} + \delta W_{int}^{m} + \delta W_{int}^{e} - \delta W_{ext}^{m} - \delta W_{ext}^{e} = 0, \quad (21)$$

for all $(\delta\boldsymbol{u}, \delta\psi) \in \boldsymbol{\mathcal{V}_0^u} \times \mathcal{V}_0^{\psi}$ where

$$\delta W_{iner} := \int_{\Omega} \rho\ddot{\boldsymbol{u}} \cdot \delta\boldsymbol{u} \, d\Omega, \tag{22a}$$

$$\delta W_{int}^{m} := \int_{\Omega} \boldsymbol{\sigma} : \delta\boldsymbol{\varepsilon} \, d\Omega, \tag{22b}$$

$$\delta W_{ext}^{m} := \int_{\Omega} \rho\boldsymbol{b} \cdot \delta\boldsymbol{u} \, d\Omega + \int_{\Gamma^{\sigma}} \boldsymbol{t} \cdot \delta\boldsymbol{u} \, d\Gamma, \tag{22c}$$

$$\delta W_{int}^{e} := -\int_{\Omega} \boldsymbol{D} \cdot \delta\boldsymbol{E} \, d\Omega, \tag{22d}$$

$$\delta W_{ext}^{e} := \int_{\Omega} \rho^{e}\delta\psi \, d\Omega + \int_{\Gamma^{D}} \omega\delta\psi \, d\Gamma, \tag{22e}$$

represent the different contributions (e.g. inertial, internal, external, mechanical, electrical) to the total virtual work and

$$\delta\boldsymbol{\varepsilon} = \frac{1}{2}\left(\nabla\delta\boldsymbol{u} + (\nabla\delta\boldsymbol{u})^{T}\right), \qquad \delta\boldsymbol{E} = -\boldsymbol{\nabla}\delta\psi. \tag{23}$$

Substituting the expressions for $\delta\boldsymbol{u}$ (19) and $\delta\psi$ (20) into equation (23) results in

$$\delta\boldsymbol{\varepsilon} = \frac{1}{2}\left[(\delta\boldsymbol{\epsilon}^{m} + \delta\boldsymbol{\kappa}^{m} \times \boldsymbol{p}) \otimes \boldsymbol{e}_3 + \boldsymbol{e}_3 \otimes (\delta\boldsymbol{\epsilon}^{m} + \delta\boldsymbol{\kappa}^{m} \times \boldsymbol{p})\right], \tag{24a}$$

$$\delta\boldsymbol{E} = -\delta\boldsymbol{\epsilon}^{e} - (\boldsymbol{e}_3 \otimes \boldsymbol{p})\delta\boldsymbol{\kappa}^{e} - \boldsymbol{\mathcal{V}} : \delta\boldsymbol{\varsigma}^{e} - \boldsymbol{\mathcal{W}} : \delta\boldsymbol{\gamma}, \tag{24b}$$

where

$$\delta\boldsymbol{\epsilon}^{m} := \frac{\partial\delta\boldsymbol{w}}{\partial x_3} + \boldsymbol{e}_3 \times \delta\boldsymbol{\theta}, \qquad \delta\boldsymbol{\kappa}^{m} := \frac{\partial\delta\boldsymbol{\theta}}{\partial x_3}, \tag{25a}$$

$$\delta\boldsymbol{\epsilon}^{e} := \frac{\partial\delta\phi}{\partial x_3}\boldsymbol{e}_3 + \delta\boldsymbol{\beta}, \qquad \delta\boldsymbol{\kappa}^{e} := \frac{\partial\delta\boldsymbol{\beta}}{\partial x_3}, \qquad \delta\boldsymbol{\varsigma}^{e} := \frac{\partial\delta\boldsymbol{\gamma}}{\partial x_3}, \tag{25b}$$

represent the virtual mechanical and electrical beam strains.

12

Substituting the expressions for $\boldsymbol{u}$ (11) and $\delta\boldsymbol{u}$ (19) into (22a) yields (after integration over the cross sectional area A) the inertial virtual work

$$\delta W_{iner} = \int_l \left[\delta\boldsymbol{w} \cdot \left(\mathbf{A}_D \ddot{\boldsymbol{w}} + \mathbf{S}_D \ddot{\boldsymbol{\theta}} \right) + \delta\boldsymbol{\theta} \cdot \left(\mathbf{S}_D^T \ddot{\boldsymbol{w}} + \mathbf{I}_D \ddot{\boldsymbol{\theta}} \right) \right] dx_3, \qquad (26)$$

where

$$\boldsymbol{A}_D := \int_A \rho \boldsymbol{I} dA, \qquad \boldsymbol{S}_D := \int_A \rho \hat{\boldsymbol{p}} \, dA, \qquad \boldsymbol{I}_D := \int_A \rho \hat{\boldsymbol{p}} \hat{\boldsymbol{p}}^T dA, \qquad (27)$$

represent the mass $\boldsymbol{A}_D$, first area moment $\boldsymbol{S}_D$ and second area moment $\boldsymbol{I}_D$ tensors of the cross sectional area A. Notice that $\hat{\boldsymbol{p}}$ represents the skew symmetric tensor associated with the position vector $\boldsymbol{p}$. When considering a reference frame whose origin coincides with the centre of mass of the cross sectional area A, then $\boldsymbol{S}_D = \boldsymbol{0}$. Moreover, if the reference frame is aligned along the so-called principal directions, the second area moment tensor $\boldsymbol{I}_D$ becomes diagonal.

Analogously, substituting the expression for $\delta\boldsymbol{\varepsilon}$ (24a) into (22b) yields (after integration over the cross sectional area A) the internal mechanical virtual work

$$\delta W_{int}^m = \int_l \left[\delta\boldsymbol{\epsilon}^m \cdot \boldsymbol{Q}^m + \delta\boldsymbol{\kappa}^m \cdot \boldsymbol{M}^m \right] dx_3, \qquad (28)$$

with

$$\boldsymbol{Q}^m := \int_A \boldsymbol{\sigma} \boldsymbol{e}_3 dA, \qquad \boldsymbol{M}^m := \int_A \boldsymbol{p} \times (\boldsymbol{\sigma} \boldsymbol{e}_3) dA. \qquad (29)$$

In above equation (28), $\boldsymbol{Q}^m$ represents the internal shear/axial force whereas $\boldsymbol{M}^m$ represents the internal bending/torsion moment.

Substituting the expression for $\delta\boldsymbol{u}$ (19) into (22c) yields (after integration over the cross sectional area A) the mechanical external virtual work

$$\delta W_{ext}^m = [\delta\boldsymbol{w} \cdot \boldsymbol{Q}^m + \delta\boldsymbol{\theta} \cdot \boldsymbol{M}^m]_0^l + \int_l [\delta\boldsymbol{w} \cdot \boldsymbol{q}^m + \delta\boldsymbol{\theta} \cdot \boldsymbol{m}^m] dx_3, \qquad (30)$$

where

$$\boldsymbol{q}^m := \int_A \rho \boldsymbol{b} dA + \int_{\partial A} \boldsymbol{t} d\Gamma, \qquad \boldsymbol{m}^m := \int_A (\boldsymbol{p} \times \rho \boldsymbol{b}) \, dA + \int_{\partial A} (\boldsymbol{p} \times \boldsymbol{t}) \, d\Gamma. \quad (31)$$

In above equations (30) and (31), $\boldsymbol{q}^m$ and $\boldsymbol{m}^m$ represent a possible external distributed force and moment, respectively, acting along the beam axis.

13

The first term in squared brackets on the right hand side of equation (30) represents mechanical actions (force and moment) applied at both ends of the beam, namely $x_3 = 0$ and $x_3 = l$.

From the electrical point of view, substituting the expression for $\delta \boldsymbol{E}$ (24b) into (22d) yields (after integration over the cross sectional area A) the internal electrical virtual work

$$\delta W_{int}^e = \int_l [\delta \boldsymbol{\epsilon}^e \cdot \boldsymbol{Q}^e + \delta \boldsymbol{\kappa}^e \cdot \boldsymbol{M}^e + \delta \boldsymbol{\varsigma}^e : \boldsymbol{O}^e + \delta \boldsymbol{\gamma} : \boldsymbol{P}^e] \, dx_3, \qquad (32)$$

where

$$\boldsymbol{Q}^e := \int_A \boldsymbol{D} dA, \qquad\qquad \boldsymbol{M}^e := \int_A (\boldsymbol{D} \cdot \boldsymbol{e}_3) \, \boldsymbol{p} \, dA, \qquad (33a)$$

$$\boldsymbol{P}^e := \int_A \boldsymbol{D} \cdot \boldsymbol{\mathcal{W}} dA, \qquad\qquad \boldsymbol{O}^e := \int_A \boldsymbol{D} \cdot \boldsymbol{\mathcal{V}} dA. \qquad (33b)$$

In above equations (32) and (33a), it is very interesting to observe the similarities between $\boldsymbol{Q}^e$ and $\boldsymbol{M}^e$ and their mechanical counterparts (29), namely $\boldsymbol{Q}^m$ and $\boldsymbol{M}^m$, respectively. In addition, due to the quadratic nature of the electric potential distribution, two extra second order tensors arise, that is $\boldsymbol{P}^e$ and $\boldsymbol{O}^e$ expressed in terms of the third order tensors $\boldsymbol{\mathcal{W}}$ and $\boldsymbol{\mathcal{V}}$ already defined in (18).

Finally, substituting the expression for $\delta \psi$ (20) into (22e) yields (after integration over the cross sectional area A) the electrical external virtual work as

$$\delta W_{ext}^e = [\delta\phi \, (\boldsymbol{Q}^e \cdot \boldsymbol{e}_3) + \delta\boldsymbol{\beta} \cdot \boldsymbol{M}^e + \delta\boldsymbol{\gamma} : \boldsymbol{O}^e]_0^l + \int_l [\delta\phi \, q^e + \delta\boldsymbol{\beta} \cdot \boldsymbol{m}^e + \delta\boldsymbol{\gamma} : \boldsymbol{o}^e] \, dx_3, \tag{34}$$

where

$$q^e := \int_A \rho^e dA + \int_{\partial A} \omega \, d\Gamma, \tag{35a}$$

$$\boldsymbol{m}^e := \int_A \rho^e \boldsymbol{p} \, dA + \int_{\partial A} \omega \boldsymbol{p} \, d\Gamma, \tag{35b}$$

$$\boldsymbol{o}^e := \int_A \frac{\rho^e}{2} (\boldsymbol{p} \otimes \boldsymbol{p}) \, dA + \int_{\partial A} \frac{\omega}{2} (\boldsymbol{p} \otimes \boldsymbol{p}) \, d\Gamma. \tag{35c}$$

Again, it is interesting to note the similarities between the above expressions q^e, $\boldsymbol{m}^e$ (35) and those of $\boldsymbol{q}^m$, $\boldsymbol{m}^m$ (31). In above equation (34), q^e,

14

$\boldsymbol{m}^e$ and $\boldsymbol{o}^e$ represent possible distributed electrical effects per unit of length. Moreover, $(\boldsymbol{Q}^e \cdot \boldsymbol{e}_3)$, $\boldsymbol{M}^e$ and $\boldsymbol{O}^e$ represent electrical actions applied at both ends of the beam, namely $x_3 = 0$ and $x_3 = L$.

For completeness, the final virtual work expression characterising the behaviour of the piezoelectric beam can be written as

Find $(\boldsymbol{u}, \psi) \in \boldsymbol{\mathcal{V}}_{\tilde{\boldsymbol{u}}}^{\boldsymbol{u}} \times \mathcal{V}_{\tilde{\psi}}^{\psi}$ such that

$$\delta W := \delta W_{iner} + \delta W_{int} - \delta W_{ext} = 0, \tag{36}$$

for all $(\delta \boldsymbol{u}, \delta \psi) \in \boldsymbol{\mathcal{V}}_{\boldsymbol{0}}^{\boldsymbol{u}} \times \mathcal{V}_{0}^{\psi}$ where

$$\delta W_{iner} = \int_l \left[\delta \boldsymbol{w} \cdot \left(\mathbf{A}_D \ddot{\boldsymbol{w}} + \mathbf{S}_D \ddot{\boldsymbol{\theta}} \right) + \delta \boldsymbol{\theta} \cdot \left(\mathbf{S}_D^T \ddot{\boldsymbol{w}} + \mathbf{I}_D \ddot{\boldsymbol{\theta}} \right) \right] dx_3, \tag{37a}$$

$$\delta W_{int} = \int_l \left[\delta \boldsymbol{\epsilon}^m \cdot \boldsymbol{Q}^m + \delta \boldsymbol{\kappa}^m \cdot \boldsymbol{M}^m \right] dx_3$$

$$+ \int_l \left[\delta \boldsymbol{\epsilon}^e \cdot \boldsymbol{Q}^e + \delta \boldsymbol{\kappa}^e \cdot \boldsymbol{M}^e + \delta \boldsymbol{\varsigma}^e : \boldsymbol{P}^e + \delta \boldsymbol{\gamma} : \boldsymbol{O}^e \right] dx_3, \tag{37b}$$

$$\delta W_{ext} = \left[\delta \boldsymbol{w} \cdot \boldsymbol{Q}^m + \delta \boldsymbol{\theta} \cdot \boldsymbol{M}^m \right]_0^l + \int_l \left[\delta \boldsymbol{w} \cdot \boldsymbol{q}^m + \delta \boldsymbol{\theta} \cdot \boldsymbol{m}^m \right] dx_3$$

$$+ \left[\delta \phi (\boldsymbol{Q}^e \cdot \boldsymbol{e}_3) + \delta \boldsymbol{\beta} \cdot \boldsymbol{M}^e + \delta \boldsymbol{\gamma} : \boldsymbol{O}^e \right]_0^l + \int_l \left[\delta \phi \, q^e + \delta \boldsymbol{\beta} \cdot \boldsymbol{m}^e + \delta \boldsymbol{\gamma} : \boldsymbol{o}^e \right] dx_3. \tag{37c}$$

5. Mechanical and electrical cross sectional balance equations

5.1. Beam balance equations

As it is well known in standard beam theory [24], further manipulation of the above variational form (36)-(37) can lead to the so-called beam balance equations, which are indeed written as,

15

$$\frac{\partial \boldsymbol{Q}^m}{\partial x_3} + \boldsymbol{q}^m = \mathbf{A}_D \ddot{\boldsymbol{w}} + \mathbf{S}_D \ddot{\boldsymbol{\theta}}, \quad \text{in} \quad l \times [0, T], \tag{38a}$$

$$\frac{\partial \boldsymbol{M}^m}{\partial x_3} - \boldsymbol{Q}^m \times \boldsymbol{e}_3 + \boldsymbol{m}^m = \mathbf{S}_D^T \ddot{\boldsymbol{w}} + \mathbf{I}_D \ddot{\boldsymbol{\theta}}, \quad \text{in} \quad l \times [0, T], \tag{38b}$$

$$\frac{\partial (\boldsymbol{Q}^e \cdot \boldsymbol{e}_3)}{\partial x_3} + q^e = 0, \quad \text{in} \quad l \times [0, T], \tag{38c}$$

$$\frac{\partial \boldsymbol{M}^e}{\partial x_3} - (\boldsymbol{I} - \boldsymbol{e}_3 \otimes \boldsymbol{e}_3) \boldsymbol{Q}^e + \boldsymbol{m}^e = \boldsymbol{0}, \quad \text{in} \quad l \times [0, T], \tag{38d}$$

$$\frac{\partial \boldsymbol{O}^e}{\partial x_3} - \boldsymbol{P}^e + \boldsymbol{o}^e = \boldsymbol{0}, \quad \text{in} \quad l \times [0, T], \tag{38e}$$

The above set of equations represent a set of balance equations in terms of internal area resultants $\boldsymbol{Q}^m$, $\boldsymbol{M}^m$, $\boldsymbol{Q}^e$, $\boldsymbol{M}^e$, $\boldsymbol{P}^e$ and $\boldsymbol{O}^e$. Initial conditions (4c-4d), boundary conditions (2a,4a), mechanical strains (12-13) and their electrical counterparts (16-17) complement the above system of partial differential equations (38) to form the initial boundary value problem of the three-dimensional piezoelectric beam. Specifically, compatible initial conditions can be defined in terms of axis varying functions $\boldsymbol{w}_0, \dot{\boldsymbol{w}}_0, \boldsymbol{\theta}_0, \dot{\boldsymbol{\theta}}_0 : [0, l] \to \mathbb{R}^3$ as

$$\boldsymbol{u}(x_1, x_2, x_3, t) = \boldsymbol{w}_0(x_3) + \boldsymbol{\theta}_0(x_3) \times \boldsymbol{p}(x_1, x_2) \quad \text{in} \quad \Omega \times 0, \tag{39a}$$

$$\dot{\boldsymbol{u}}(x_1, x_2, x_3, t) = \dot{\boldsymbol{w}}_0(x_3) + \dot{\boldsymbol{\theta}}_0(x_3) \times \boldsymbol{p}(x_1, x_2) \quad \text{in} \quad \Omega \times 0, \tag{39b}$$

Dirichlet (and corresponding Neumann) boundary conditions can be defined at either end of the beam $x_3 = 0$ or $x_3 = l$ by

$$\boldsymbol{w} = \bar{\boldsymbol{w}}, \qquad \boldsymbol{\theta} = \bar{\boldsymbol{\theta}}, \qquad \phi = \bar{\phi}, \qquad \boldsymbol{\beta} = \bar{\boldsymbol{\beta}}, \qquad \boldsymbol{\gamma} = \bar{\boldsymbol{\gamma}}, \tag{40a}$$

$$\boldsymbol{Q}^m = \bar{\boldsymbol{Q}}^m, \quad \boldsymbol{M}^m = \bar{\boldsymbol{M}}^m, \quad \boldsymbol{Q}^e \cdot \boldsymbol{e}_3 = \bar{Q}^e, \quad \boldsymbol{M}^e = \bar{\boldsymbol{M}}^e, \quad \boldsymbol{O}^e = \bar{\boldsymbol{O}}^e. \tag{40b}$$

Naturally, wherever a Dirichlet boundary condition is defined, a corresponding Neumann boundary condition cannot be used. Finally, in order to close the system defined by (12-13), (38), (39) and (40), it is necessary to establish relationships between the internal area resultants and the mechanical/electrical strains.

5.2. Internal area resultants

From the mechanical standpoint, having introduced the additive decomposition of the total Cauchy stress tensor $\boldsymbol{\sigma}$ in equation (7), we now proceed

to find the traction vector acting in a cross sectional area A of the beam defined by the outward unit normal $\boldsymbol{e}_3$, namely $\boldsymbol{\sigma}\boldsymbol{e}_3$. For the mechanical contribution $\boldsymbol{\sigma}^m$, combining equations (7) and (12), it yields

$$\boldsymbol{\sigma}^m\boldsymbol{e}_3 = \boldsymbol{\Xi}(\boldsymbol{\epsilon}^m + \hat{\boldsymbol{p}}^T\boldsymbol{\kappa}^m), \qquad [\boldsymbol{\Xi}]_{ij} = [\boldsymbol{\mathcal{C}}]_{ikjl}[\boldsymbol{e}_3]_k[\boldsymbol{e}_3]_l. \tag{41}$$

Analogously, for the electrical contribution $\boldsymbol{\sigma}^e$, combining equations (7) and (16), it yields

$$\boldsymbol{\sigma}^e\boldsymbol{e}_3 = \boldsymbol{\Theta}\left(\boldsymbol{\epsilon}^e + (\boldsymbol{e}_3 \otimes \boldsymbol{p})\boldsymbol{\kappa}^e + \boldsymbol{\mathcal{V}} : \boldsymbol{\varsigma}^e + \boldsymbol{\mathcal{W}} : \boldsymbol{\gamma}\right), \qquad [\boldsymbol{\Theta}]_{ij} = [\boldsymbol{\mathcal{P}}]_{jik}[\boldsymbol{e}_3]_k. \tag{42}$$

The first internal area resultant $\boldsymbol{Q}^m$, also known as the axial/shear force, can now be computed from equations (29), (41) and (42) as

$$\boldsymbol{Q}^m = \boldsymbol{A}^m\boldsymbol{\epsilon}^m + \boldsymbol{S}^m\boldsymbol{\kappa}^m + \boldsymbol{A}_1^e\boldsymbol{\epsilon}^e + \boldsymbol{S}_1^e\boldsymbol{\kappa}^e + \boldsymbol{S}_2^e : \boldsymbol{\gamma} + \boldsymbol{I}_1^e : \boldsymbol{\varsigma}^e, \tag{43}$$

where

$$\boldsymbol{A}^m := \int_A \boldsymbol{\Xi}\, dA, \qquad \boldsymbol{S}^m := \int_A \boldsymbol{\Xi}\hat{\boldsymbol{p}}^T dA, \qquad \boldsymbol{A}_1^e := \int_A \boldsymbol{\Theta} dA,$$

$$\boldsymbol{S}_1^e := \int_A \boldsymbol{\Theta}(\boldsymbol{e}_3 \otimes \boldsymbol{p})dA, \qquad \boldsymbol{I}_1^e := \int_A \boldsymbol{\Theta}\boldsymbol{\mathcal{V}} dA, \qquad \boldsymbol{S}_2^e := \int_A \boldsymbol{\Theta}\boldsymbol{\mathcal{W}} dA,$$

The first two terms on the right hand side of (43) stem from strain contributions whereas the remainder stem from electrical contributions. The second internal area resultant $\boldsymbol{M}^m$, also known as bending/torsion moment, can also be computed from equations (29), (41) and (42) as

$$\boldsymbol{M}^m = (\boldsymbol{S}^m)^T \boldsymbol{\epsilon}^m + \boldsymbol{I}^m\boldsymbol{\kappa}^m + \boldsymbol{S}_3^e\boldsymbol{\epsilon}^e + \boldsymbol{I}_2^e\boldsymbol{\kappa}^e + \boldsymbol{I}_3^e : \boldsymbol{\gamma} + \boldsymbol{G}_1^e : \boldsymbol{\varsigma}^e, \tag{45}$$

where

$$\boldsymbol{I}^m := \int_A \hat{\boldsymbol{p}}\boldsymbol{\Xi}\hat{\boldsymbol{p}}^T dA, \qquad \boldsymbol{S}_3^e := \int_A \hat{\boldsymbol{p}}\boldsymbol{\Theta} dA, \qquad \boldsymbol{I}_2^e := \int_A \hat{\boldsymbol{p}}\boldsymbol{\Theta}(\boldsymbol{e}_3 \otimes \boldsymbol{p})dA,$$

$$\boldsymbol{G}_1^e := \int_A \hat{\boldsymbol{p}}\boldsymbol{\Theta}\boldsymbol{\mathcal{V}} dA, \qquad \boldsymbol{I}_3^e := \int_A \hat{\boldsymbol{p}}\boldsymbol{\Theta}\boldsymbol{\mathcal{W}} dA.$$

From the electrical standpoint, having introduced the additive decomposition of the electric displacement $\boldsymbol{D}$ in equation (6), we can obtain after combining equations (6), (12) and (16)

$$\boldsymbol{D}^m = \boldsymbol{\Theta}^T(\boldsymbol{\epsilon}^m + \hat{\boldsymbol{p}}^T\boldsymbol{\kappa}^m), \tag{47}$$

17

and
$$\boldsymbol{D}^e = -\boldsymbol{\epsilon}(\boldsymbol{\epsilon}^e + (\boldsymbol{e}_3 \otimes \boldsymbol{p})\boldsymbol{\kappa}^e + \boldsymbol{\mathcal{V}} : \boldsymbol{\varsigma}^e + \boldsymbol{\mathcal{W}} : \boldsymbol{\gamma}). \tag{48}$$

The third internal area resultant $\boldsymbol{Q}^e$ can now be computed from equations (33a), (47) and (48) as

$$\boldsymbol{Q}^e = (\boldsymbol{A}_1^e)^T \boldsymbol{\epsilon}^m + (\boldsymbol{S}_3^e)^T \boldsymbol{\kappa}^m - \boldsymbol{A}_2^e \boldsymbol{\epsilon}^e - \boldsymbol{S}_4^e \boldsymbol{\kappa}^e - \boldsymbol{S}_5^e : \boldsymbol{\gamma} - \boldsymbol{I}_4^e : \boldsymbol{\varsigma}^e, \tag{49}$$

where

$$\boldsymbol{A}_2^e := \int_A \boldsymbol{\epsilon}\, dA, \qquad\qquad \boldsymbol{S}_4^e := \int_A \boldsymbol{\epsilon}(\boldsymbol{e}_3 \otimes \boldsymbol{p})\, dA,$$
$$\boldsymbol{I}_4^e := \int_A \boldsymbol{\epsilon}\boldsymbol{\mathcal{V}}\, dA, \qquad\qquad \boldsymbol{S}_5^e := \int_A \boldsymbol{\epsilon}\boldsymbol{\mathcal{W}}\, dA.$$

Analogously, the fourth $\boldsymbol{M}^e$, fifth $\boldsymbol{P}^e$ and sixth $\boldsymbol{O}^e$ internal area resultants can be computed from equations (33a-33b), (47) and (48) as

$$\boldsymbol{M}^e = (\boldsymbol{S}_1^e)^T \boldsymbol{\epsilon}^m + (\boldsymbol{I}_2^e)^T \boldsymbol{\kappa}^m - (\boldsymbol{S}_4^e)^T \boldsymbol{\epsilon}^e - \boldsymbol{I}_5^e \boldsymbol{\kappa}^e - \boldsymbol{I}_6^e : \boldsymbol{\gamma} - \boldsymbol{G}_2^e : \boldsymbol{\varsigma}^e,$$
$$\boldsymbol{P}^e = (\boldsymbol{S}_2^e)^T \boldsymbol{\epsilon}^m + (\boldsymbol{I}_3^e)^T \boldsymbol{\kappa}^m - (\boldsymbol{S}_5^e)^T \boldsymbol{\epsilon}^e - (\boldsymbol{I}_6^e)^T \boldsymbol{\kappa}^e - \boldsymbol{I}_7^e : \boldsymbol{\gamma} - \boldsymbol{G}_3^e : \boldsymbol{\varsigma}^e,$$
$$\boldsymbol{O}^e = (\boldsymbol{I}_1^e)^T \boldsymbol{\epsilon}^m + (\boldsymbol{G}_1^e)^T \boldsymbol{\kappa}^m - (\boldsymbol{I}_4^e)^T \boldsymbol{\epsilon}^e - (\boldsymbol{G}_2^e)^T \boldsymbol{\kappa}^e - (\boldsymbol{G}_3^e)^T : \boldsymbol{\gamma} - \boldsymbol{J}^e : \boldsymbol{\varsigma}^e,$$
$$\tag{51}$$

where

$$\boldsymbol{I}_5^e := \int_A (\boldsymbol{p} \otimes \boldsymbol{e}_3)\boldsymbol{\epsilon}(\boldsymbol{e}_3 \times \boldsymbol{p})\, dA, \quad \boldsymbol{J}^e := \int_A \boldsymbol{\mathcal{V}}^{*T}\boldsymbol{\epsilon}\boldsymbol{\mathcal{V}}\, dA, \quad \boldsymbol{I}_6^e := \int_A (\boldsymbol{p} \otimes \boldsymbol{e}_3)\boldsymbol{\epsilon}\boldsymbol{\mathcal{W}}\, dA,$$
$$\boldsymbol{G}_2^e := \int_A (\boldsymbol{p} \otimes \boldsymbol{e}_3)\boldsymbol{\epsilon}\boldsymbol{\mathcal{V}}\, dA, \qquad\qquad \boldsymbol{G}_3^e := \int_A \boldsymbol{\mathcal{W}}^{*T}\boldsymbol{\epsilon}\boldsymbol{\mathcal{V}}\, dA, \quad \boldsymbol{I}_7^e := \int_A \boldsymbol{\mathcal{W}}^{*T}\boldsymbol{\epsilon}\boldsymbol{\mathcal{W}}\, dA.$$

Finally, we can summarise all of the above relationships between internal area resultants and mechanical/electrical strains in the following table matrix format[6]

---

[6]Notice that the entries in columns one to four correspond to second order tensors whereas the entries in columns five and six correspond to third order tensors.

18

$$
\begin{bmatrix} \boldsymbol{Q}^m \\ \boldsymbol{M}^m \\ \boldsymbol{Q}^e \\ \boldsymbol{M}^e \\ \boldsymbol{P}^e \\ \boldsymbol{O}^e \end{bmatrix} = \begin{bmatrix} \boldsymbol{A}^m & \boldsymbol{S}^m & \boldsymbol{A}_1^e & \boldsymbol{S}_1^e & \boldsymbol{S}_2^e & \boldsymbol{I}_1^e \\ & \boldsymbol{I}^m & \boldsymbol{S}_3^e & \boldsymbol{I}_2^e & \boldsymbol{I}_3^e & \boldsymbol{G}_1^e \\ & & -\boldsymbol{A}_2^e & -\boldsymbol{S}_4^e & -\boldsymbol{S}_5^e & -\boldsymbol{I}_4^e \\ & & & -\boldsymbol{I}_5^e & -\boldsymbol{I}_6^e & -\boldsymbol{G}_2^e \\ & & & & -\boldsymbol{I}_7^e & -\boldsymbol{G}_3^e \\ Sym & & & & & -\boldsymbol{J}^e \end{bmatrix} \begin{bmatrix} \boldsymbol{\varepsilon}^m \\ \boldsymbol{\kappa}^m \\ \boldsymbol{\varepsilon}^e \\ \boldsymbol{\kappa}^e \\ :\boldsymbol{\gamma} \\ :\boldsymbol{\varsigma}^e \end{bmatrix} . \quad (53)
$$

As expected, the resulting matrix is symmetric and has a saddle point structure due to its derivation from the enthalpy density of the system. In the case of dealing with a homogeneous material across the section of the beam, namely constant mechanical and electrical properties within the area section A, if the origin of the reference triad $\{\boldsymbol{e}_1, \boldsymbol{e}_2, \boldsymbol{e}_3\}$ is chosen as the centre of mass of the section, then the tensors $\boldsymbol{S}^m$, $\boldsymbol{S}_k^e$ ($k = 1 \ldots 5$) and $\boldsymbol{G}_k^e$ ($k = 1 \ldots 3$) vanish (e.g. their integrand is of odd order in the position vector $\boldsymbol{p}$). Finally, we note that the initial boundary value problem representing the behaviour of a piezoelectric three-dimensional beam is defined by equations (12), (13), (38), (39), (40) and (53).

6. Analytical solution of planar piezoelectric beams

The aim of this section is to present closed-form solutions for some particular cases of piezoelectric beams, which will enable the benchmarking of the finite element implementation presented in a subsequent section of this paper. In addition, the presentation of closed-form solutions is of interest to prospective researchers in order to validate their piezoelectric beam models. To the best of our knowledge, closed-form solutions of two-way coupled piezoelectric beams with quadratic distribution of electric potential within the cross section do not exist in the literature.

We will focus on the analysis of two-dimensional beams (placed on the plane defined by Ox_1x_3) where distributed effects along the beam will be disregarded (i.e. $\boldsymbol{q}^m = \boldsymbol{0}$, $\boldsymbol{m}^m = \boldsymbol{0}$, $q^e = 0$, $\boldsymbol{m}^e = \boldsymbol{0}$, $\boldsymbol{o}^e = \boldsymbol{0}$) and we will seek solutions to static problems where inertial terms are neglected (e.g. $\rho = 0$). In addition, we will particularise our solutions to beams with homogeneous cross sectional area where the origin of the reference frame coincides with the centre of mass of the section.

For simplicity, the displacement $\boldsymbol{w}$ of the cross sectional reference frame origin is considered perpendicular to the beam axis, namely $\boldsymbol{w}\cdot\boldsymbol{e}_3 = 0$, and no torsion along the beam axis is considered either, $\boldsymbol{\theta} \cdot \boldsymbol{e}_3 = 0$. In this case, the

19

problem is fully described by the following five variables $\{w := \boldsymbol{w} \cdot \boldsymbol{e}_1,\ \theta := \boldsymbol{\theta} \cdot \boldsymbol{e}_2,\ \phi,\ \beta := \boldsymbol{\beta} \cdot \boldsymbol{e}_1,\ \gamma := \boldsymbol{e}_1 \cdot \boldsymbol{\gamma} \cdot \boldsymbol{e}_1\} : [0, l] \to \mathbb{R}$. Substitution of equations (53) into the beam balance equations (38) yields, after redefinition of the beam coordinate axis as $x \in [0, l]$,

$$a_1 \left(\frac{dw}{dx} - \theta \right) + a_2 \beta + a_3 \frac{d\phi}{dx} + \frac{a_{14}}{2} \frac{d\gamma}{dx} = \bar{Q}^m, \quad (54a)$$

$$a_4 \frac{d^2\theta}{dx^2} - a_5 \frac{d^2\beta}{dx^2} - a_{15} \frac{d\gamma}{dx} + a_1 \left(\frac{dw}{dx} - \theta \right) + a_2 \beta + a_3 \frac{d\phi}{dx} + \frac{a_{14}}{2} \frac{d\gamma}{dx} = 0, \quad (54b)$$

$$a_6 \left(\frac{dw}{dx} - \theta \right) - a_7 \beta - a_8 \frac{d\phi}{dx} - \frac{a_{16}}{2} \frac{d\gamma}{dx} = \bar{Q}^e, \quad (54c)$$

$$a_9 \frac{d^2\theta}{dx^2} + a_{10} \frac{d^2\beta}{dx^2} + \frac{a_{17}}{2} \frac{d\gamma}{dx} + a_{11} \left(\frac{dw}{dx} - \theta \right) - a_{12} \beta - a_{13} \frac{d\phi}{dx} = 0, \quad (54d)$$

$$\frac{d}{dx} \left[\frac{a_{18}}{2} \left(\frac{dw}{dx} - \theta \right) - \frac{1}{2} \left(a_{19} \beta + a_{20} \frac{d\phi}{dx} \right) - \frac{a_{21}}{4} \frac{d\gamma}{dx} \right]$$
$$+ a_{22} \frac{d\theta}{dx} + a_{23} \frac{d\beta}{dx} + a_{24} \gamma = 0, \quad (54e)$$

where coefficients a_k $(k = 1 \ldots 24)$, expressed in terms of mechanical, electrical and geometrical properties, are defined as

$$
\begin{aligned}
&a_1 := \mu A\, k_s, & &a_2 := \mathcal{P}_{113} A\, k_s, & &a_3 := \mathcal{P}_{313} A\, k_s, & &a_4 := EI, \\
&a_5 := \mathcal{P}_{333} I, & &a_6 := \mathcal{P}_{313} A, & &a_7 := \epsilon_{13} A, & &a_8 := \epsilon_{33} A, \\
&a_9 := \mathcal{P}_{333} I, & &a_{10} := \epsilon_{33} I, & &a_{11} := \mathcal{P}_{113} A, & &a_{12} := \epsilon_{11} A, \\
&a_{13} := \epsilon_{13} A, & &a_{14} := \mathcal{P}_{313} I, & &a_{15} := \mathcal{P}_{133} I, & &a_{16} := \epsilon_{33} I, \\
&a_{17} := \epsilon_{13} I, & &a_{18} := \mathcal{P}_{313} I, & &a_{19} := \epsilon_{13} I, & &a_{20} := \epsilon_{33} I, \\
&a_{21} := \epsilon_{33} J, & &a_{22} := \mathcal{P}_{133} I, & &a_{23} := \epsilon_{13} I, & &a_{24} := \epsilon_{11} I,
\end{aligned}
$$

where A is the cross sectional area, $I := \int_A (x_1)^2 dA$ is the second moment of area of the section, $J := \int_A (x_1)^4 dA$ is the fourth moment of area of the section, E is the Young modulus, μ is the shear modulus, $\mathcal{P}_{ijk}$ are piezoelectric coefficients and ϵ_{ij} are dielectric coefficients. k_s represents a shear factor correction for the section [24] that will be taken as one unless otherwise stated. Together with appropriate boundary conditions (40), the piezoelectric beam problem is completely closed with the above set of equations (54). Note that

20

we have assumed that all material and geometric beam properties remain constant throughout the beam length.

The set of boundary conditions considered for a cantilever problem are

$$w = 0, \qquad \theta = 0, \quad \phi = 0, \qquad \beta = 0, \quad \gamma = 0, \quad \text{at } x = 0, \quad (55\text{a})$$
$$Q^m = \bar{Q}^m, \quad M^m = 0, \quad Q^e = \bar{Q}^e, \quad M^e = 0, \quad O^e = 0, \quad \text{at } x = l, \quad (55\text{b})$$

where $Q^m := \boldsymbol{Q}^m \cdot \boldsymbol{e}_1$, $M^m := \boldsymbol{M}^m \cdot \boldsymbol{e}_2$, $Q^e := \boldsymbol{Q}^e \cdot \boldsymbol{e}_3$, $M^e := \boldsymbol{M}^e \cdot \boldsymbol{e}_1$ and $O^e := \boldsymbol{e}_1 \cdot \boldsymbol{O}^e \boldsymbol{e}_1$. As it is common in piezoelectric beam literature [1, 19, 21], for the electrical part we have postulated similar Dirichlet and Neumann boundary conditions to those of the mechanical problem i.e. all electric variables are zero at the fixed end and the derivatives are specified at the free end in a coupled fashion. From (54a) and (54c) we can deduce $\left(\frac{dw}{dx} - \theta\right)$ and $\frac{d\phi}{dx}$ as

$$\left(\frac{dw}{dx} - \theta\right) = \frac{\bar{Q}^m}{a_1} - \frac{a_2}{a_1}\beta - \frac{a_3}{a_1}\frac{d\phi}{dx} - \frac{1}{2}\frac{a_{14}}{a_1}\frac{d\gamma}{dx}, \qquad (56\text{a})$$

$$\frac{d\phi}{dx} = \frac{a_6}{a_1 b_2}\bar{Q}^m - \frac{\bar{Q}^e}{b_2} - \frac{b_1}{b_2}\beta - \frac{b_8}{b_2}\frac{d\gamma}{dx}, \qquad (56\text{b})$$

where coefficients b_1, b_2 and b_8 are defined in Appendix A. After back substitution into (54b), (54d) and (54e), we obtain

$$a_4\frac{d^2\theta}{dx^2} - a_5\frac{d^2\beta}{dx^2} - a_{15}\frac{d\gamma}{dx} + \bar{Q}^m = 0, \qquad (57\text{a})$$

$$a_9\frac{d^2\theta}{dx^2} + a_{10}\frac{d^2\beta}{dx^2} + b_9\frac{d\gamma}{dx} - b_5\beta + b_6\bar{Q}^m + b_7\bar{Q}^e = 0, \qquad (57\text{b})$$

$$\frac{d^2\gamma}{dx^2} + k_1^2\gamma + m_1\frac{d\beta}{dx} + m_3\frac{d\theta}{dx} = 0, \qquad (57\text{c})$$

where coefficients b_5, b_6, b_7, b_9, m_1, m_1, m_3 and k_1 are defined in Appendix A. The above three equations (57), together with relevant boundary conditions, can be integrated to solve for θ, β and γ. Then, by using equations in (56), the remaining variables w and ϕ can be obtained.

The solution of these equations would require four piezoelectric parameters $\mathcal{P}_{113}$, $\mathcal{P}_{133}$, $\mathcal{P}_{313}$ and $\mathcal{P}_{333}$, three dielectric parameters ϵ_{11}, ϵ_{13} and ϵ_{33} and two mechanical parameters μ and E. From a practical viewpoint, piezoelectric materials having all of the above material parameters non-zero are rare and the solution obtained using this approach would be too lengthy to be reported. For such closed-form solutions, the reader can refer to Poya [16].

We identify two practically feasible scenarios for the above set of differential equations (57). Firstly, the case where the electric potential distribution is assumed to vary linearly within the cross section. Secondly, the case where the electric potential distribution is assumed to vary quadratically within the cross section but the electric permittivity tensor ϵ is considered to be diagonal and the piezoelectric component $\mathcal{P}_{133} = 0$. The most notable piezoelectric materials, such as PZT-5H, PZT-5A, Quartz and many others, share these features.

6.1. Linear electric potential distribution within the cross section

In this case, the equations in (57) reduce to

$$a_4\frac{d^2\theta}{dx^2} - a_5\frac{d^2\beta}{dx^2} + \bar{Q}^m = 0, \tag{58a}$$

$$a_9\frac{d^2\theta}{dx^2} + a_{10}\frac{d^2\beta}{dx^2} - b_5\beta + b_6\bar{Q}^m + b_7\bar{Q}^e = 0, \tag{58b}$$

with the following set of boundary conditions

$$\theta|_{x=0} = 0, \qquad\qquad \beta|_{x=0} = 0, \tag{59a}$$

$$\left.\frac{d\theta}{dx}\right|_{x=l} = 0, \qquad\qquad \left.\frac{d\beta}{dx}\right|_{x=l} = 0. \tag{59b}$$

The final closed-form solution of this problem yields

$$\beta(x) := \frac{(\bar{Q}^m b_3 + \bar{Q}^e b_4)}{k^2} \, g(x),$$

$$\phi(x) := \left(\frac{\bar{Q}^m a_6}{a_1 b_2} - \frac{\bar{Q}^e}{b_2}\right) x - \frac{b_1(\bar{Q}^m b_3 + \bar{Q}^e b_4)}{b_2 \, k^3} f(x),$$

$$\theta(x) := \frac{\bar{Q}^m l x}{a_4} - \frac{\bar{Q}^m x^2}{2a_4} + \frac{a_5(\bar{Q}^m b_3 + \bar{Q}^e b_4)}{a_4 k^2} g(x),$$

$$w(x) := \left[\frac{\bar{Q}^m}{a_1} + \frac{a_3(\bar{Q}^e a_1 - \bar{Q}^m a_6)}{a_1^2 b_2}\right] x + \frac{\bar{Q}^m L x^2}{2a_4} - \frac{\bar{Q}^m x^3}{6a_4} + \left(\bar{Q}^m b_3 + \bar{Q}^e b_4\right) h(x),$$

$$f(x) := \frac{\sinh(kl - kx) - \sinh(kl) + kx \cosh(kl)}{\cosh(kl)},$$

$$g(x) := 1 - \frac{\cosh(kl - kx)}{\cosh(kl)},$$

$$h(x) := \frac{(a_1 a_5 b_2 - a_2 a_4 b_2 + a_3 a_4 b_1)\left[\sinh(kl - kx) - \sinh(kl) + kx \cosh(kl)\right]}{a_1 a_4 b_2 k^3 \cosh(kl)},$$

where the new coefficients b_3, b_4 and k are defined in Appendix A.

6.2. Quadratic electric potential distribution within the cross section

In the case of quadratic electric potential distribution, a diagonal electric permittivity tensor and piezoelectric component $\mathcal{P}_{133} = 0$, which is the case for a major class of piezoceramics [31] and, specifically, the ones used in piezoelectric beam literature [6, 10, 5, 1, 3, 8, 9, 21], the three differential equations (57) take the form,

$$a_4 \frac{d^2\theta}{dx^2} - a_5 \frac{d^2\beta}{dx^2} + \bar{Q}^m = 0, \tag{60a}$$

$$a_9 \frac{d^2\theta}{dx^2} + a_{10} \frac{d^2\beta}{dx^2} - b_5\beta + b_6\bar{Q}^m + b_7\bar{Q}^e = 0, \tag{60b}$$

$$\frac{d^2\gamma}{dx^2} + k_1^2\gamma + m_1 \frac{d\beta}{dx} = 0, \tag{60c}$$

with the following set of boundary conditions,

$$\theta|_{x=0} = 0, \qquad \beta|_{x=0} = 0, \qquad \gamma|_{x=0} = 0, \tag{61a}$$

$$\left.\frac{d\theta}{dx}\right|_{x=l} = 0, \qquad \left.\frac{d\beta}{dx}\right|_{x=l} = 0, \qquad \left.\frac{d\gamma}{dx}\right|_{x=l} = m_2, \tag{61b}$$

23

where m_2 is a coefficient which depends on the electromechanical loading and the electric gradient β at $x = l$, as given in Appendix A. The final closed form of this problem is defined for the electrical variables as

$$\phi(x) := \left(\frac{\bar{Q}^m a_6}{a_1 b_2} - \frac{\bar{Q}^e}{b_2} \right) x + f_1(x) + f_2(x) + f_3(x) + f_4(x) + f_5(x),$$

$$\beta(x) := \frac{(\bar{Q}^m b_3 + \bar{Q}^e b_4)}{k^2} \left[1 - \frac{\cosh(kl - kx)}{\cosh(kl)} \right],$$

$$\gamma(x) := \frac{m_2 \sinh(k_1 x) \left(k^2 - k_1^2 \right)}{\cosh(k_1 l) \left(k^2 k_1 - k_1^3 \right)} + \frac{m_1 (\bar{Q}^m b_3 + \bar{Q}^e b_4) \sinh(kl - k x)}{\cosh(kl) \left(k k_1^2 - k^3 \right)} + f_6(x),$$

$$f_1(x) := -\frac{b_1 \left(\bar{Q}^m b_3 + \bar{Q}^e b_4 \right)}{b_2} \left[\frac{\sinh(kl - kx) + kx \cosh(kl) - \sinh(kl)}{k^3 \cosh(kl)} \right],$$

$$f_2(x) := -\frac{b_8}{b_2} \left[\frac{m_2 \sinh(k_1 x) \left(k^2 - k_1^2 \right)}{\cosh(k_1 l) \left(k^2 k_1 - k_1^3 \right)} + \frac{m_1 \left(\bar{Q}^m b_3 + \bar{Q}^e b_4 \right) \sinh(kl - kx)}{\cosh(kl) \left(k k_1^2 - k^3 \right)} \right],$$

$$f_3(x) := -\frac{b_8 m_1 \left(\bar{Q}^m b_3 + \bar{Q}^e b_4 \right)}{b_2} \left[\frac{2k \sinh(k_1 x) - \sinh(kl) \left(e^{(kl + 2k_1 x)} + k_1 e^{k_1 (l-x)} \right)}{2 \cosh(kl) \cosh(k_1 l) \left(k k_1^3 - k^3 k_1 \right)} \right],$$

$$f_4(x) := \frac{b_8 m_1 \left(\bar{Q}^m b_3 + \bar{Q}^e b_4 \right)}{b_2} \left[\frac{\sinh(kl)}{\cosh(kl) \left(k k_1^2 - k^3 \right)} \right],$$

$$f_5(x) := -\frac{b_8 m_1 \left(\bar{Q}^m b_3 + \bar{Q}^e b_4 \right)}{b_2} \left[\frac{\sinh(kl) \left(e^{kl} + k_1 e^{k_1 l} \right)}{2 \cosh(kl) \cosh(k_1 l) \left(k k_1^3 - k^3 k_1 \right)} \right],$$

$$f_6(x) := \frac{m_1 \left(\bar{Q}^m b_3 + \bar{Q}^e b_4 \right) \left[2k \sinh(k_1 x) - \sinh(kl) \left(e^{(kl + 2k_1 x)} + k_1 e^{k_1 (l-x)} \right) \right]}{2 \cosh(kl) \cosh(k_1 l) \left(k k_1^3 - k^3 k_1 \right)},$$

and for the mechanical variables as

24

$$\theta(x) := \frac{\bar{Q}^m l x}{a_4} - \frac{\bar{Q}^m\, x^2}{2\, a_4} + \frac{a_5\left(\bar{Q}^m b_3 + \bar{Q}^e b_4\right)}{a_4 k^2}\left[1 - \frac{\cosh(kl - kx)}{\cosh(kl)}\right],$$

$$w(x) := \frac{\bar{Q}^m x}{a_1} + \frac{\bar{Q}^m l x^2}{2a_4} - \frac{\bar{Q}^m x^3}{6\, a_4} + \frac{a_5\left(\bar{Q}^m b_3 + \bar{Q}^e b_4\right) x}{a_4\, k^2} + g_1(x) + g_2(x) + g_3(x)$$
$$+ g_4(x) + g_5(x) + g_6(x) + g_7(x) + g_8(x) + g_9(x) + g_{10}(x) + g_{11}(x) + g_{12}(x),$$

$$g_1(x) := \frac{a_5\left(\bar{Q}^m b_3 + \bar{Q}^e b_4\right)\left[\sinh(kl - kx) - \sinh(kl)\right]}{a_4\, k^3\, \cosh(kl)},$$

$$g_2(x) := -\frac{a_2\left(\bar{Q}^m b_3 + \bar{Q}^e b_4\right)}{a_1}\left[\frac{\sinh(kl - kx) + kx\cosh(kl) - \sinh(kl)}{k^3\, \cosh(kl)}\right],$$

$$g_3(x) := -\frac{a_3}{a_1}\left(\frac{a_6 \bar{Q}^m}{a_1 b_2} - \frac{\bar{Q}^e}{b_2}\right) x,$$

$$g_4(x) := \frac{a_3 b_1\left(\bar{Q}^m b_3 + \bar{Q}^e b_4\right)}{a_1 b_2}\left[\frac{\sinh(kl - kx) + kx\cosh(kl) - \sinh(kl)}{k^3\, \cosh(kl)}\right],$$

$$g_5(x) := \frac{a_3 b_8}{a_1 b_2}\left[\frac{m_2\, \sinh(k_1 x)\left(k^2 - k_1{}^2\right)}{\cosh(k_1 l)\left(k^2 k_1 - k_1{}^3\right)} + \frac{m_1\left(\bar{Q}^m b_3 + \bar{Q}^e b_4\right)\sinh(kl - kx)}{\cosh(kl)\left(k\, k_1{}^2 - k^3\right)}\right],$$

$$g_6(x) := -\frac{a_3 b_8 m_1\left(\bar{Q}^m b_3 + \bar{Q}^e b_4\right)}{a_1 b_2}\frac{\left[2k\sinh(k_1 x) - \sinh(kl)\left(\mathrm{e}^{(kl + 2k_1 x)} + k_1\, \mathrm{e}^{k_1\,(l - x)}\right)\right]}{2\, \cosh(kl)\,\cosh(k_1 l)\left(k\, k_1{}^3 - k^3 k_1\right)},$$

$$g_7(x) := \frac{a_3 b_8 m_1\left(\bar{Q}^m b_3 + \bar{Q}^e b_4\right)}{a_1 b_2}\left[\frac{\sinh(kl)\left(\mathrm{e}^{kl} + k_1 \mathrm{e}^{k_1 l}\right)}{2\, \cosh(kl)\,\cosh(k_1 l)\left(k\, k_1{}^3 - k^3 k_1\right)}\right],$$

$$g_8(x) := -\frac{a_3 b_8 m_1\left(\bar{Q}^m b_3 + \bar{Q}^e b_4\right)}{a_1 b_2}\left[\frac{\sinh(kl)}{\cosh(kl)\left(k\, k_1{}^2 - k^3\right)}\right],$$

$$g_9(x) := -\frac{a_{14}}{2\, a_1}\left[\frac{m_2\, \sinh(k_1 x)\left(k^2 - k_1{}^2\right)}{\cosh(k_1 l)\left(k^2 k_1 - k_1{}^3\right)} + \frac{m_1\left(\bar{Q}^m b_3 + \bar{Q}^e b_4\right)\sinh(kl - kx)}{\cosh(kl)\left(k\, k_1{}^2 - k^3\right)}\right],$$

$$g_{10}(x) := -\frac{a_{14} m_1\left(\bar{Q}^m b_3 + \bar{Q}^e b_4\right)}{2\, a_1}\left[\frac{2k\sinh(k_1 x) - \sinh(kl)\left(\mathrm{e}^{(kl + 2k_1 x)} + k_1\, \mathrm{e}^{k_1(l - x)}\right)}{2\, \cosh(kl)\,\cosh(k_1 l)\left(k\, k_1{}^3 - k^3 k_1\right)}\right],$$

$$g_{11}(x) := \frac{a_{14} m_1\left(\bar{Q}^m b_3 + \bar{Q}^e b_4\right)}{2\, a_1}\left[\frac{\sinh(kl)}{\cosh(kl)\left(k\, k_1{}^2 - k^3\right)}\right],$$

$$g_{12}(x) := -\frac{a_{14} m_1\left(\bar{Q}^m b_3 + \bar{Q}^e b_4\right)}{2\, a_1}\left[\frac{\sinh(kl)\left(\mathrm{e}^{kl} + k_1\, \mathrm{e}^{k_1 l}\right)}{2\, \cosh(kl)\,\cosh(k_1 l)\left(k\, k_1{}^3 - k^3 k_1\right)}\right],$$

where the new coefficients m_1 and k are defined in Appendix A.

7. The Finite Element Discretisation

The finite element discretisation of (36) follows naturally by introducing a non–overlapping partition of l into a series of one–dimensional elements. In particular, we choose to employ the hp-version of the finite element method as it is known to overcome the problems of locking associated with low-order approaches [26, 27, 28]. We introduce a set of H^1 conforming interpolatory functions, $\mathcal{V}_{hp} \subset H^1(\Omega)$, where the subscript h refers to the mesh spacing and p to the polynomial degree. In the hp-finite element method it is possible to construct a discretisation where the order of the elements varies throughout the mesh but, in our case, we adopt the simplest configuration and fix the polynomial degree to be uniform. The corresponding discrete weak variational statement is: Find $(\boldsymbol{u}_{hp}, \psi_{hp}) \in \boldsymbol{\mathcal{V}}_{\bar{\boldsymbol{u}}}^{\boldsymbol{u}} \cap \boldsymbol{\mathcal{V}}_{hp}^{\boldsymbol{u}} \times \mathcal{V}_{\bar{\psi}}^{\psi} \cap \mathcal{V}_{hp}^{\psi}$ such that

$$\delta W := \delta W_{iner} + \delta W_{int} - \delta W_{ext} = 0, \tag{62}$$

for all $(\delta\boldsymbol{u}_{hp}, \delta\psi_{hp}) \in \boldsymbol{\mathcal{V}}_{\boldsymbol{0}}^{\boldsymbol{u}} \cap \boldsymbol{\mathcal{V}}_{hp}^{\boldsymbol{u}} \times \mathcal{V}_0^{\psi} \cap \mathcal{V}_{hp}^{\psi}$ where

$$\boldsymbol{\mathcal{V}}_{hp}^{\boldsymbol{u}} := \{\boldsymbol{u}_{hp} \mid \boldsymbol{u}_{hp} := \boldsymbol{w}_{hp} + \boldsymbol{\theta}_{hp} \times \boldsymbol{p}\}, \tag{63}$$

$$\mathcal{V}_{hp}^{\psi} := \left\{\psi_{hp} \mid \psi_{hp} := \phi_{hp} + \boldsymbol{p} \cdot \boldsymbol{\beta}_{hp} + \frac{1}{2}\boldsymbol{p} \cdot \boldsymbol{\gamma}_{hp} \cdot \boldsymbol{p}\right\}, \tag{64}$$

with the component functions $\{(\boldsymbol{w}_{hp}\cdot\boldsymbol{e}_i), (\boldsymbol{\theta}_{hp}\cdot\boldsymbol{e}_i), \phi_{hp}, (\boldsymbol{\beta}_{hp}\cdot\boldsymbol{e}_\alpha), (\boldsymbol{e}_\alpha\cdot\boldsymbol{\gamma}_{hp}\boldsymbol{e}_\beta)\} \in \mathcal{V}_{hp}$.

Discussions of suitable sets of hierarchic basis functions for $\mathcal{V}_{hp}$, which have implementation advantages over standard Lagrangian nodal basis functions, can be found in a range of texts (e.g. [32, 33, 34]) and, therefore, will not be discussed further here. For details of the numerical treatment of these elements, and our specific implementation, we refer to the aforementioned references and [16].

8. Numerical examples

The numerical examples presented in this section have been carried out using FEAPB, a cross-platform hp-finite element analysis program for piezo-electric beams [35], developed based on the theoretical formulation outlined

in this paper and distributed as a free software under the terms of GNU General Public License at https://github.com/romeric/FEAPB.

The piezoelectric material properties used in Examples 8.1 and 8.2 are presented below in Voigt notation and taken from [3]. Note that for shear actuator problems, the electric permittivity tensor is not required since the problem is purely mechanical.

$$\mathcal{C} = \begin{bmatrix} 126 & 79.5 & 84.1 & 0 & 0 & 0 \\ 79.5 & 126 & 84.1 & 0 & 0 & 0 \\ 84.1 & 84.1 & 117 & 0 & 0 & 0 \\ 0 & 0 & 0 & 23.3 & 0 & 0 \\ 0 & 0 & 0 & 0 & 23.3 & 0 \\ 0 & 0 & 0 & 0 & 0 & 23.25 \end{bmatrix} GPa,$$

$$\epsilon = \begin{bmatrix} 1.505 & 0 & 0 \\ 0 & 1.505 & 0 \\ 0 & 0 & 1.3 \end{bmatrix} 10^{-8} \frac{C}{Vm},$$

$$\mathcal{P} = \begin{bmatrix} 0 & 0 & 0 & 0 & 17 & 0 \\ 0 & 0 & 0 & 17 & 0 & 0 \\ -6.5 & -6.5 & 23.3 & 0 & 0 & 0 \end{bmatrix} \frac{C}{m^2}.$$

The material properties of AT-cut Quartz, of density $\rho = 2649 \frac{kg}{m^3}$, used in Example 8.3, are given below [31].

$$\mathcal{C} = \begin{bmatrix} 86.74 & -8.25 & 27.15 & -3.66 & 0 & 0 \\ & 129.77 & -7.42 & 5.7 & 0 & 0 \\ & & 102.83 & 9.92 & 0 & 0 \\ & & & 38.61 & 0 & 0 \\ & & & & 68.81 & 2.53 \\ sym & & & & & 29.01 \end{bmatrix} \times 10^9 \frac{N}{m^2},$$

$$\epsilon = \begin{bmatrix} 39.21 & 0 & 0 \\ & 39.82 & 0.86 \\ sym & & 40.42 \end{bmatrix} \times 10^{-12} \frac{C}{Vm},$$

$$\mathcal{P} = \begin{bmatrix} 0.171 & 0 & 0 \\ -0.152 & 0 & 0 \\ -0.0187 & 0 & 0 \\ 0.067 & 0 & 0 \\ 0 & 0.108 & -0.0761 \\ 0 & -0.095 & 0.067 \end{bmatrix} \frac{C}{m^2}.$$

In order to benchmark the *hp*-finite element scheme proposed, we define for a tensor (e.g. scalar, vector or second order) field $\boldsymbol{\zeta} : [0, l] \times t \rightarrow \mathbb{R}^n$, where n is the dimension of the tensor field, the following L^2 and H^1 norms

$$
\begin{aligned}
\|\boldsymbol{\zeta}\|_{L^2} &:= \left[\int_l \boldsymbol{\zeta} : \boldsymbol{\zeta} \, dx_3 \right]^{1/2}, \\
\|\boldsymbol{\zeta}\|_{H^1} &:= \left[\int_l \left(\boldsymbol{\zeta} : \boldsymbol{\zeta} + \frac{\partial \boldsymbol{\zeta}}{\partial x_3} : \frac{\partial \boldsymbol{\zeta}}{\partial x_3} \right) dx_3 \right]^{1/2},
\end{aligned}
\tag{65}
$$

associated with the magnitude of the tensor field $\boldsymbol{\zeta}$. In our case, $\boldsymbol{\zeta}$ can be any of the mechanical and electrical unknowns, namely $\boldsymbol{w}$, $\boldsymbol{\theta}$, ϕ, $\boldsymbol{\beta}$ and $\boldsymbol{\gamma}$. In addition, the following energy norm can be defined

$$
\|\boldsymbol{\pi}\|_E := \left[\int_l \frac{1}{2} \left(\boldsymbol{\varepsilon}^m \cdot \boldsymbol{Q}^m + \boldsymbol{\kappa}^m \cdot \boldsymbol{M}^m + \boldsymbol{\varepsilon}^e \cdot \boldsymbol{Q}^e + \boldsymbol{\kappa}^e \cdot \boldsymbol{Q}^e + \boldsymbol{\varsigma}^e : \boldsymbol{P}^e + \boldsymbol{\gamma}^e \cdot \boldsymbol{O}^e \right) dx_3 \right]^{1/2},
\tag{66}
$$

where $\boldsymbol{\pi}$ gathers all the mechanical and electrical unknowns. This enables the definition of the following error norms $\|\boldsymbol{\zeta}_{hp} - \boldsymbol{\zeta}\|_{L^2} / \|\boldsymbol{\zeta}\|_{L^2}$, $\|\boldsymbol{\zeta}_{hp} - \boldsymbol{\zeta}\|_{H^1} / \|\boldsymbol{\zeta}\|_{H^1}$ and $\|\boldsymbol{\pi}_{hp} - \boldsymbol{\pi}\|_E / \|\boldsymbol{\pi}\|_E$, which can then be used to assess the convergence of the algorithm under *h*- or *p*-refinement.

8.1. The benchmark problem

To begin our numerical examples, we first benchmark the finite element implementation against the analytical solution provided in Section 6 and Appendix A. The example considered for the benchmark problem is a two dimensional cantilever beam, of height $1mm$ and length $10mm$, under the action of a unit tip load $\bar{Q}^m = 1N$ and zero electric displacement resultant $\bar{Q}^e = 0C$. The beam is assumed to be of a single fibre polarised along the length as shown in Figure 4, with material properties as given above.
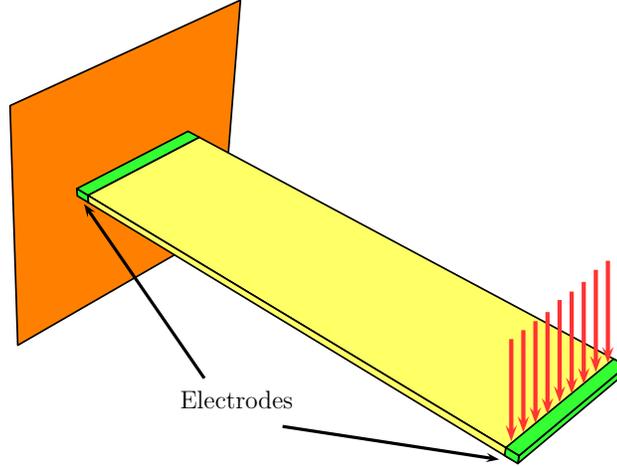
Figure 4: Cantilever beam polarised along the length

To quantify the error incurred in all the variables $\{w, \theta, \phi, \beta, \gamma\}$ of the finite element implementation, we compute the L^2, H^1 and energy norms of the error (as described above) for various mesh sizes and polynomial enhancements. In Figures 5 and 6, each line represents a fixed polynomial degree p and each data point on a given line represents a mesh size h. Unless otherwise stated, for this analysis, the basis functions of degree $p = 1, 2, 3, 4$ with equally-spaced mesh sizes have been used namely $h = 0.4, 0.2, 0.133, 0.1$ which correspond to 25, 50, 75 and 100 elements, respectively.

For hp-refinement, we put emphasis on the case of quadratic electric potential distribution within the cross section whose closed-form solution is provided in subsection 6.2. The solution for a linear electric potential distribution model can be considered as a special case of the quadratic one for which we only list the tip values of non-zero variables, $\{w, \theta, \beta\}$ and their point-wise percentage error, see Table 1 and 2. Also note that for the quadratic case *only*, to get non-zero γ and ϕ and show their convergence, we tune an additional piezoelectric parameter i.e. $\mathcal{P}_{333} = 20C/m^2$. In the following plots, slope indicates the rate of convergence. The absolute relative L^2 norm of the error in all the variables is shown in Figure 5.

Table 1: Convergence of Numerical Scheme for Tip Values

hp-Refinement	$w_{x=L}\,(mm)$	$\theta_{x=L}\,(rad)$	$\beta_{x=L}\,(rad)$
$h=5,\,p=1$	0.019382	0.002871	20.090531
$h=5,\,p=2$	0.034576	0.005128	47.566588
$h=5,\,p=3$	0.034623	0.005128	35.849481
Exact	0.034623	0.005128	35.849481

Table 2: Point-wise % Error Incurred in Table 1

hp-Refinement	% Error w	% Error θ	% Error β
$h=5,\,p=1$	44.018998	44.019046	43.958656
$h=5,\,p=2$	0.134194	4.550137e-05	32.684178
$h=5,\,p=3$	8.161727e-07	2.385000e-12	4.784048e-07

These convergence rates are in good agreement with theoretical predictions [33, 34]. In fact, in some cases, the convergence rate is far superior, for instance, as it can be observed in the convergence of the electric potential (Figure 5b) with quadratic basis function $p = 2$. The stagnation in convergence occurs when the numerical solution reaches the analytical solution (Figure 5a), which normally happens at a higher value than the computer language floating-point precision.

A similar trend is observed with the convergence of the H^1 norm of the error, shown in Figure 6. Again, the convergence rate is in agreement with theoretical predictions [33].

To further elaborate the overall convergence of the problem, we compute the energy norm of the error for both linear and quadratic electric potential distributions, but this time with a fixed mesh size and uniformly increased interpolation degree. In other words, we report the energy norm of the error with p-refinement, as shown in Figure 7. In addition, by means of the error measured in the energy norm, we also compare the convergence of the problem and the ability to overcome locking by increasing the degree of interpolation.

This is an important advantage of hp-finite element analysis and, although well known in the context of linear elasticity [33, 28, 29], we believe to the best of our knowledge it is missing in the piezoelectric literature.
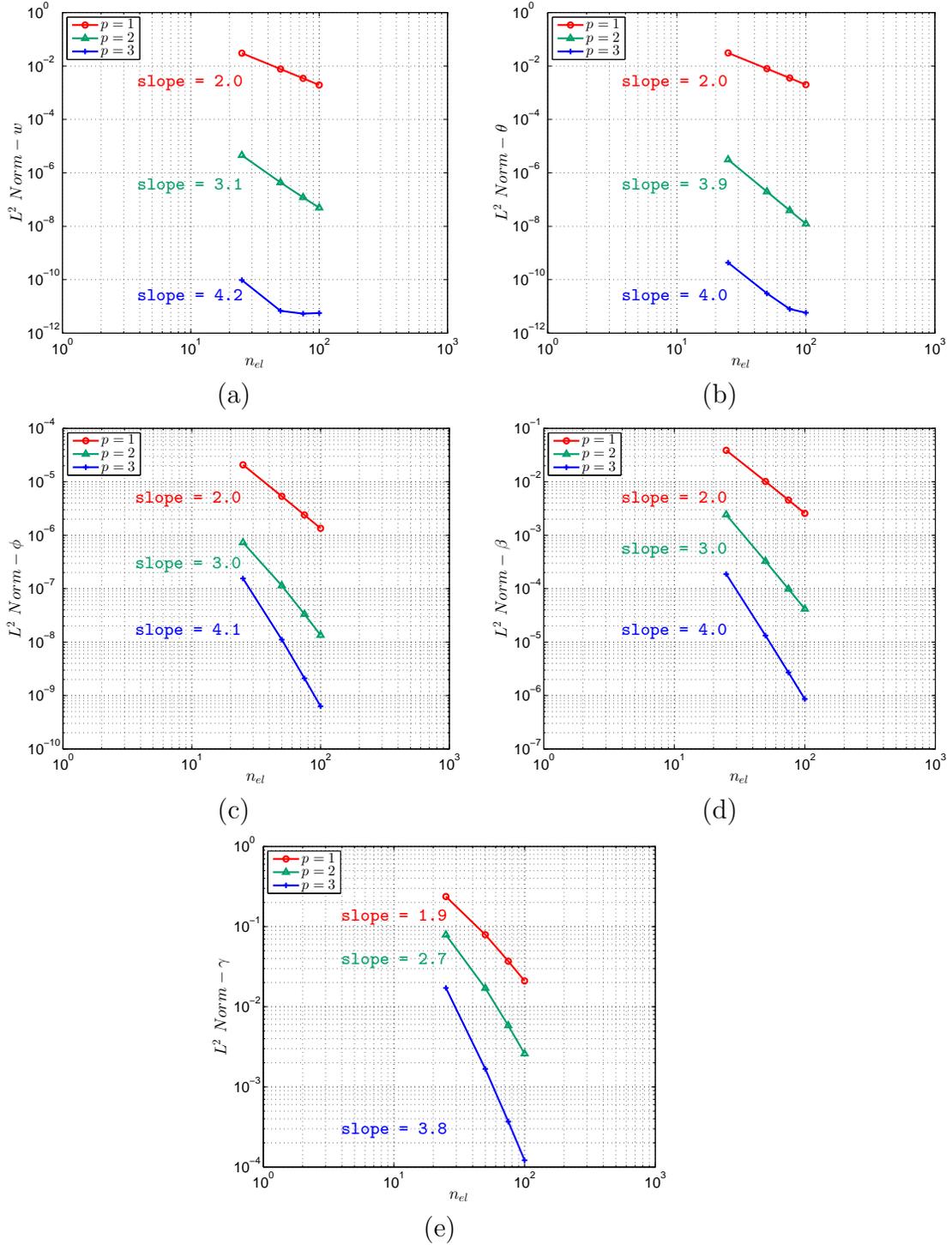
Figure 5: Convergence of the error measured in the L^2 norm for the variables (a) w; (b) θ; (c) ϕ; (d) β; (e) γ

31
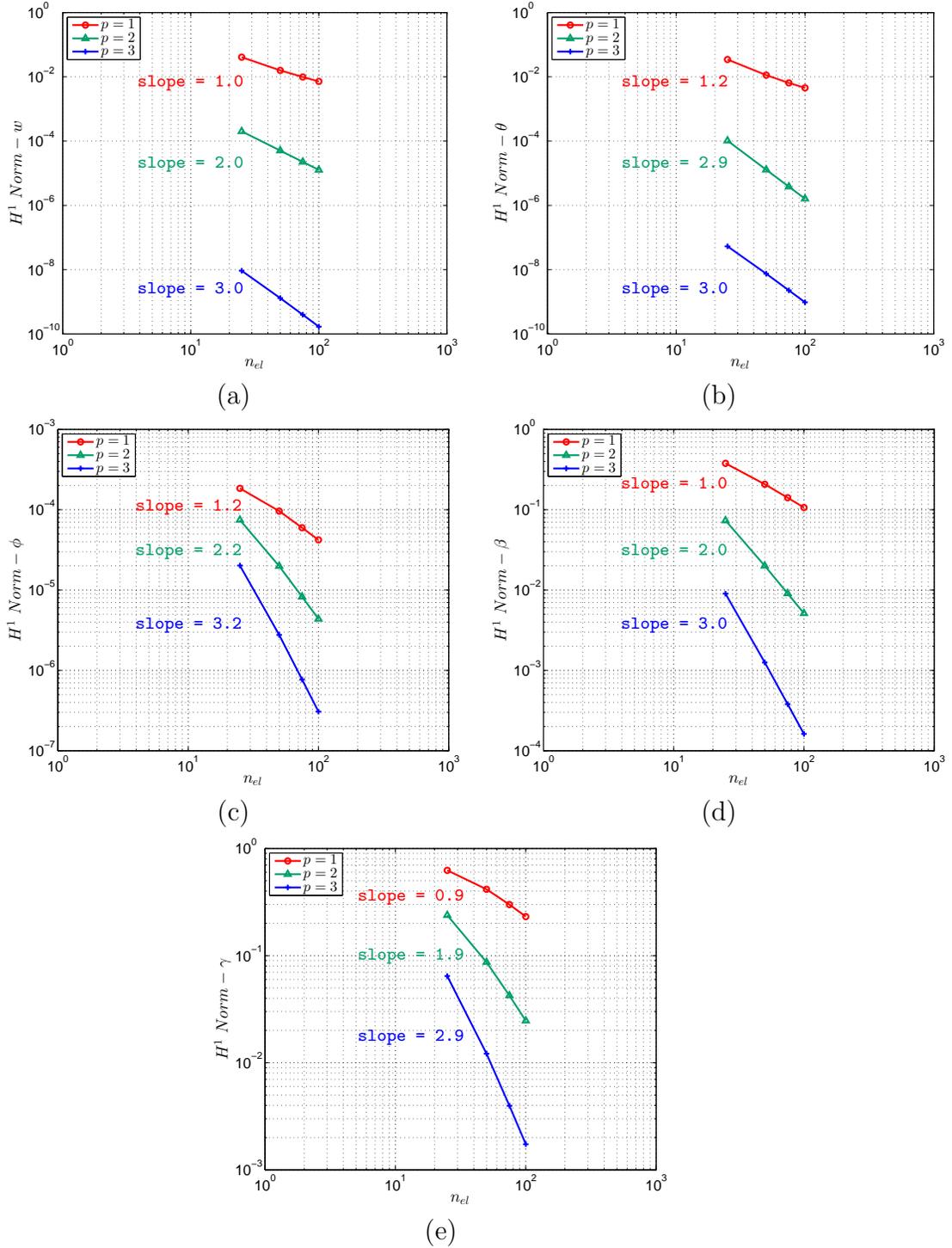
Figure 6: Convergence of the error measured in the H^1 norm for the variables (a) w; (b) θ; (c) ϕ; (d) β; (e) γ

32
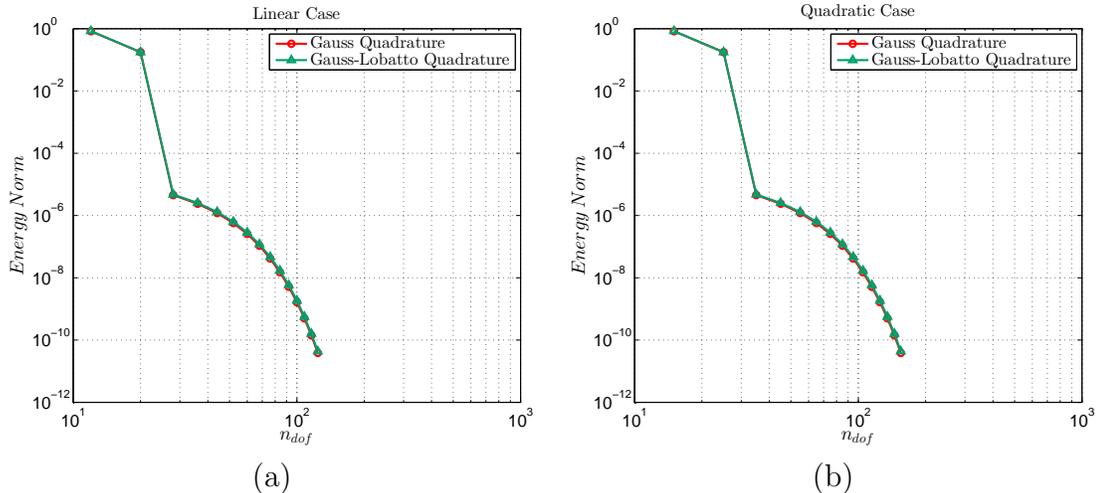
Figure 7: Convergence of the energy norm of the error under *p*-refinement and with different numerical integration techniques. (a) Linear electric potential distribution. (b) Quadratic electric potential distribution.

8.2. Shear actuator problem

In this example, we consider a composite piezoelectric beam that has a well-established solution. The shear actuator initially proposed by Zhang and Sun [2] has been analysed analytically in [2, 4], numerically in [4, 3, 19] and experimentally in [36]. In our presentation, we wish to make the distinction that our approach, unlike the majority of these models, is not restricted to actuation-only scenarios. Indeed, the proposed beam model incorporates electrical degrees of freedom and hence can also be applied to energy harvesting scenarios. In fact, shear actuator models which consider all composite layers as Timoshenko beams, can be regarded as a special case of the present formulation. For instance, the closed form solutions presented in [4] are based on equations (38a) and (38b).

The presented results correspond to when the shear actuator is analysed in a two-dimensional setting where the width of the beam is assumed to be $1mm$, the length of the beam as $100mm$, thickness of piezoelectric layer as $2mm$ and thickness of each Aluminum layer as $8mm$ [2], as shown in Figure 8. Piezoelectric material properties are given above. The modulus of elasticity and Poisson's ratio of Aluminum are 70.3 GPa and 0.345, respectively.

33
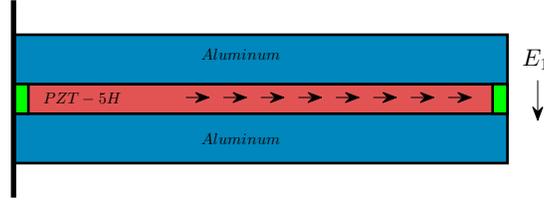
Figure 8: Geometry of the shear actuator

Although shown here in a cantilever setting, the shear actuator has also been analysed for various other mechanical end boundary conditions, such as clamped-clamped and clamped-hinged situations, for instance by Aldraihem [4]. The electric loading corresponds to an electric field E_1 of $10V/mm$ applied perpendicular to the polarisation direction, as shown in Figure 8. In our setting, this requires prescribing all the electric degrees of freedom with a value of $\beta = 10V/mm$ and zero for the rest of the electrical unknowns in all nodes.

The cross-sectional properties of the composite beam are calculated numerically, which also makes the present finite element formulation amenable to multi-layer composites and non-rectangular geometries. In the following, finite element solutions are compared with the analytical solutions provided by [4] for a Timoshenko model, for all the aforementioned boundary conditions. The beam is discretised with 20 quadratic elements.

It should be pointed out that Zhang and Sun [2] and Benjeddou et al. [3] model the non-electroactive layers of the shear actuator as an Euler-Bernoulli beam, which further requires imposing compatibility constraints in the interface between the various layers. Following [4], for a Timoshenko model, a shear factor of $k_s = 2/3$ or less is required to capture the results of the Euler-Bernoulli model, as shown in Figure 9d. For the purpose of comparison a shear factor of $5/6$ has been used in the rest of the test cases shown in Figure 9.
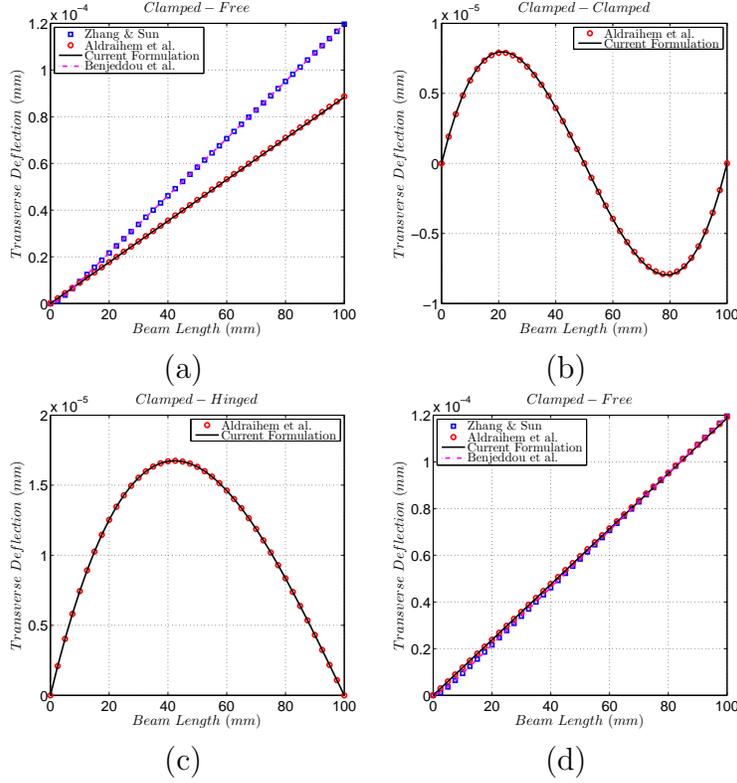
Figure 9: Transverse deflection obtained with various models (Shear factor $k_s = 5/6$). (a) Clamped-free; (b) Clamped-clamped; (c) Clamped-hinged; (d) Clamped-free with shear factor $k_s = 0.62$.

8.3. Ambient vibration energy harvester undergoing coupled bending-torsion

In this example, we analyse a fully three-dimensional piezoelectric energy harvesting beam undergoing coupled bending-torsion vibration. As reported in [10], coupled bending-torsion energy harvesters can function on broader frequency ranges and are advantageous in improving the efficiency of energy harvesting. To this effect, we analyse a fibre of AT-cut Quartz with material properties as given above and dimensions defined by length $40mm$, height $0.9mm$ and width $12mm$.

To start with, we first compute some selected natural frequencies of the beam. The dimensions of the beam are chosen such that one of these modes (i.e. sixth mode) correspond to twisting. To obtain the natural frequencies, we employ 50 elements of degree $p = 3$. Unless otherwise stated, the results reported here are with second order electric potential distribution across the

cross section. The natural frequencies corresponding to modes 1, 2, 3 and 6 are listed in Table 3 and hardly vary with respect to those corresponding to purely mechanical beam problem without any piezoelectric interaction. Hence,the natural frequencies can be verified with closed-form formulas, for instance those provided in [37]. Many researchers [1, 5, 6, 10] tend to place a point mass at the tip of the beam in order to reduce the frequency spectrum. We have opted for using directly the frequencies as obtained from the eigenvalue analysis of the beam problem.

Table 3: Natural frequencies of bending-torsion fibre (Hz)

Mode (i)	1	2	3	6
Frequency (f_i)	17.897759	111.999935	224.776362	1006.096205

The mode shapes corresponding to these frequencies are shown in Figure 10. Note that for the purpose of plotting, the interior degrees of freedom are condensed out and the colours in the plot, which essentially show the absolute magnitude of mode deformation, are magnified appropriately.
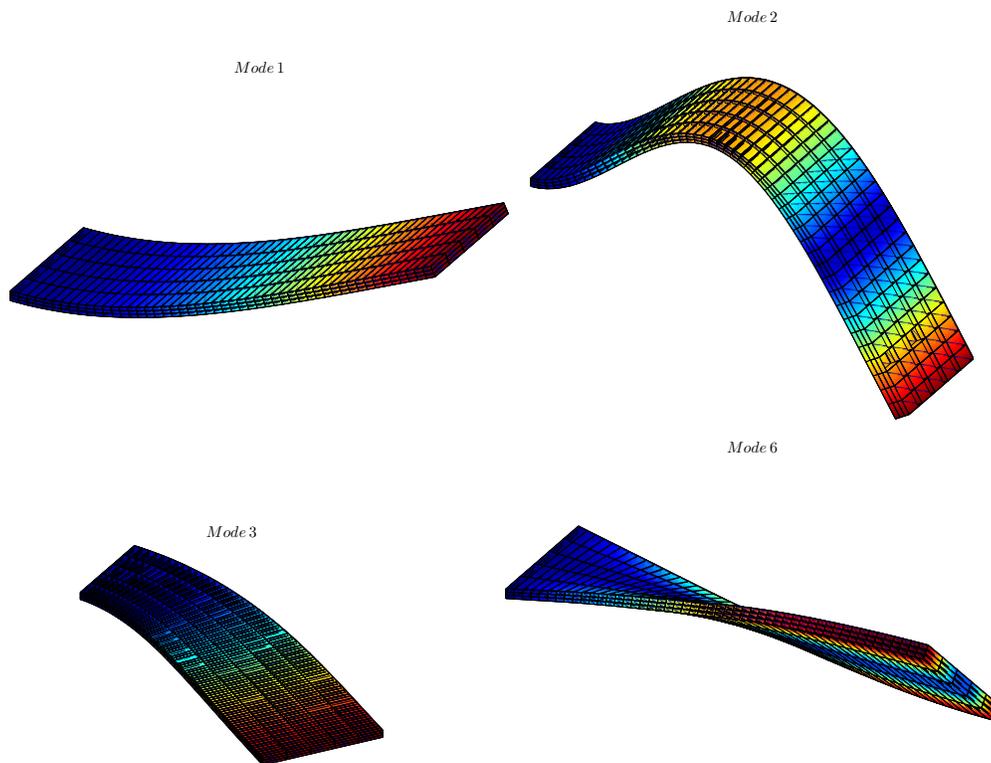
Figure 10: Selected modes of bending-torsion fibre

Once the fundamental modes of the piezoelectric fibre have been computed, we perform static analyses and compare the results obtained by using first order and second order electric potential distribution within the cross section. We categorise the results into three cases, bending only, torsion only and coupled bending-torsion. The loading scenarios are listed in Table 4, where a negative sign indicates downward loading and a positive moment stands for clockwise rotation. Loads and moments are applied at the tip.

Table 4: Loading Scenarios for Bending-Torsion Harvester

Cases/ Load	$\boldsymbol{Q}^m \cdot \boldsymbol{e}_1$ (N)	$\boldsymbol{M}^m \cdot \boldsymbol{e}_3$ (Nmm)
Case 1 - Bending	-5	0
Case 2 - Torsion	0	150
Case 3 - Bending-Torsion	-5	150

The resulting electric potential is plotted in Figure 11. Note that, while

37

the potential produced between end electrodes can be high for sensor application, our aim here is to find optimum electric output for energy harvesting purposes.
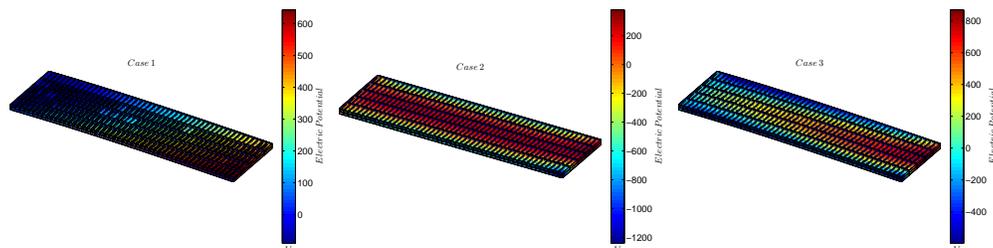
Figure 11: Voltage Output for Three Loading Cases

To demonstrate how the results vary with the consideration of a linear or quadratic electrical potential distribution across the cross section of the beam, we compute the variation of the electric potential ψ at the tip cross section and compare it through the height and through the thickness for both cases.

(a)

(b)
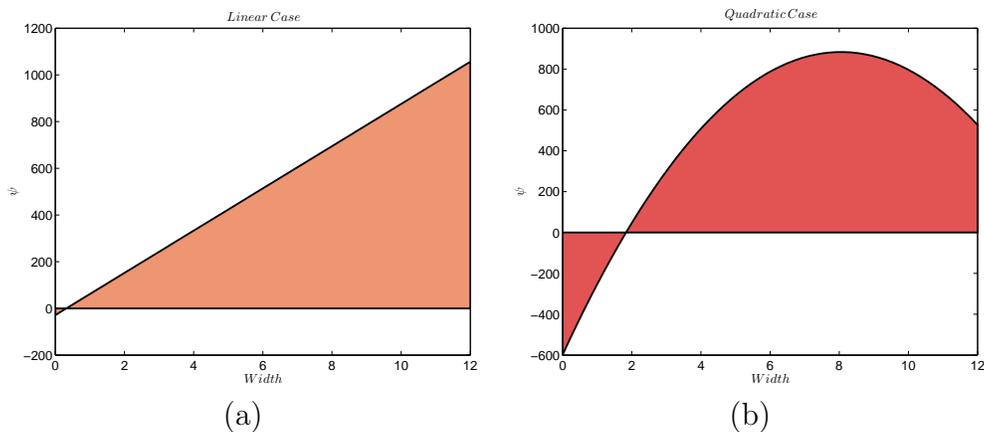
Figure 12: Variation of electric potential across the width. (a) Linear electric potential distribution. (b) Quadratic electric potential distribution.
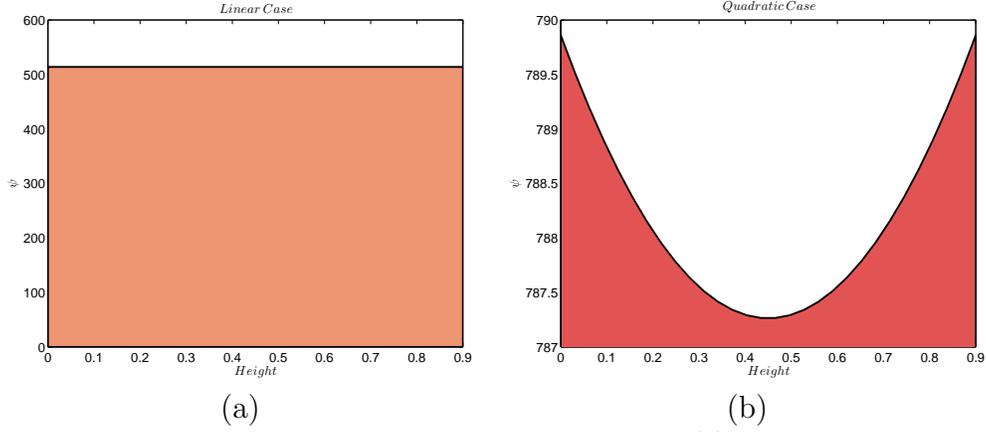
Figure 13: Variation of electric potential across the height. (a) Linear electric potential distribution. (b) Quadratic electric potential distribution.

Observe that the variation of the electric potential across the height is constant in the linear electrical potential distribution case, due to $\boldsymbol{\beta} \cdot \boldsymbol{e}_1$ being zero. In the case of quadratic electrical potential distribution, the Hessian contribution $\boldsymbol{e}_1 \cdot \boldsymbol{\gamma} \boldsymbol{e}_1$ is small across the height. The differences between cases (a) and (b) for Figures 12 and 13 are expected, as the coupling mechanisms certainly differ in different directions.

Finally, a dynamic analysis is carried out, where the beam is subjected to a harmonic end point load. The frequency of excitation of the external forcing term is chosen sequentially equal to $\omega_p \in [0.01, 0.1, 1.0, 10.0]$ rad/s. While it is possible to excite the beam at different resonance frequencies, this would lead to irreproducible results from the experimental standpoint, due to the high value of the natural frequencies. In order to obtain a bounded solution, a damped system is introduced where classical Rayleigh damping [25] is used. The damping matrix $\boldsymbol{C}$ is obtained as a linear combination of the mass $\boldsymbol{M}$ and stiffness matrices $\boldsymbol{K}$, namely $\boldsymbol{C} = a\boldsymbol{M} + b\boldsymbol{K}$, where $a = b = 0.01$ are used for this analysis.

The damped system subjected to the external forcing term is then solved via the Newmark's method using 50 quadratic elements of Lagrange-Gauss-Lobbato basis functions and the time-step size is chosen as $1/500$ s. An external forcing term defined by $\boldsymbol{Q}^m \cdot \boldsymbol{e}_1 = P_0 \sin(\omega_P t)$ is applied at the tip, where ω_P is the natural frequency of excitation (as listed above) and P_0 the amplitude of the excitation chosen in this case as 100N. Figure 14 shows the time history of the external forcing term when $\omega_P = 10 \text{rad}/sec$. Note that the external force $\omega_P = 0.01 \text{rad}/sec$ corresponds to a pulse loading.

39

As can be observed, the external forcing term is applied for the first 30s and then removed (see Figure 14). The correct consideration of the multiple degrees of freedom of the system enables the accurate capturing of the energy of the beam model, superseding alternative approaches based on simplified structural models.
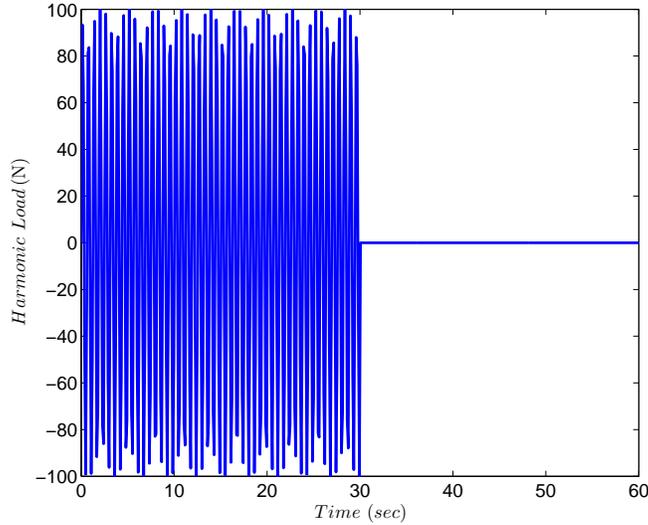
Figure 14: Harmonic vibration with frequency $\omega_p = 10$ rad/sec

The instantaneous electrical power P^e can be computed (refer to equation (32)) as

$$P^e = \int_l \left(\dot{\boldsymbol{\epsilon}}^e \cdot \boldsymbol{Q}^e + \dot{\boldsymbol{\kappa}}^e \cdot \boldsymbol{M}^e + \dot{\boldsymbol{\varsigma}}^e : \boldsymbol{P}^e + \dot{\boldsymbol{\gamma}}^e : \boldsymbol{O}^e \right) \mathrm{d}x_3. \qquad (67)$$

In the finite element context, one needs to compute the electrical power at each time step by carrying out the normal post-processing used in stress recovery (i.e. perform numerical integration to obtain the desired quantity at Gauss points, while looping over elements). Due to the linear nature of the problem, the time derivative of the electrical variables (needed to evaluate P^e) can be computed directly from the Newmark's method, without the need to resort to an ad-hoc numerical differentiation within every time step. Recall that whilst velocities and accelerations are part of the unknowns of the dynamic problem, the time rates of the electrical variables are not. The harvested power for the case of the damped system is shown in Figure 15, for the four different excitation frequencies listed above.

It should be noted that this power corresponds to an instantaneous power where it is assumed that the electrodes are not attached to an external resistor. In all the cases, the power history decreases dramatically after 30s, which is when the external forcing term is removed.

9. Conclusion

In this work, a complete three-dimensional linear piezoelectric beam formulation and its hp-finite element implementation has been presented. A Timoshenko model, used to describe the kinematics of a straight axis beam, is complemented with a quadratic description of the electric potential across the cross section of the beam. The formulation is suitable to deal with static, modal and dynamic actuation and harvesting scenarios. Starting from the continuum level, a very clear description of the beam balance equations is presented by means of the introduction of suitable mechanical (and electrical counterparts) stress and strain resultants defined along the beam axis.

The paper includes the closed-form solution for a two-dimensional piezo-electric cantilever beam, subjected to static end tip mechanical and electrical loads, and used to benchmark the numerical simulations through the use of suitable L^2, H^1 and energy error norms. In addition, the formulation has been also compared against existing literature [2, 4, 3] yielding excellent agreement in all cases. For shear-driven problems, a shear factor of 0.62 is suggested for the Timoshenko based solution in order to comply with that of layer-wise Euler-Bernoulli's approaches.
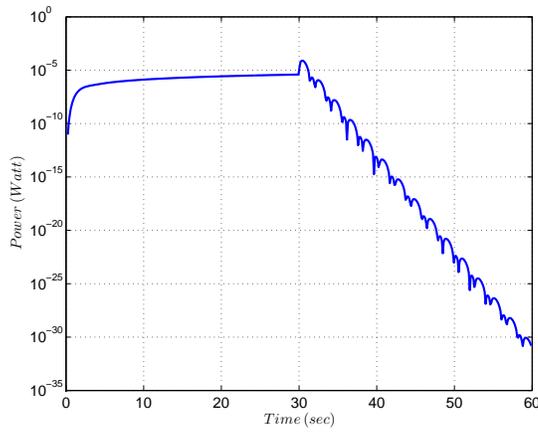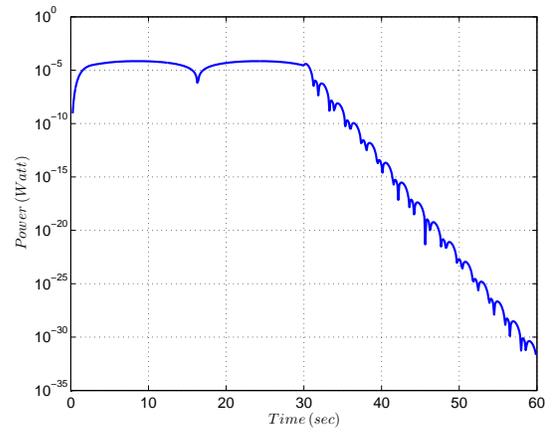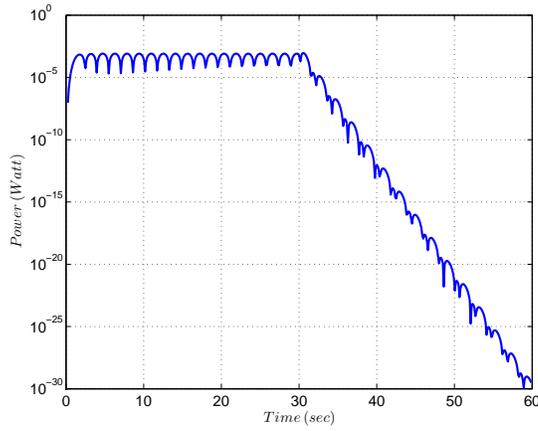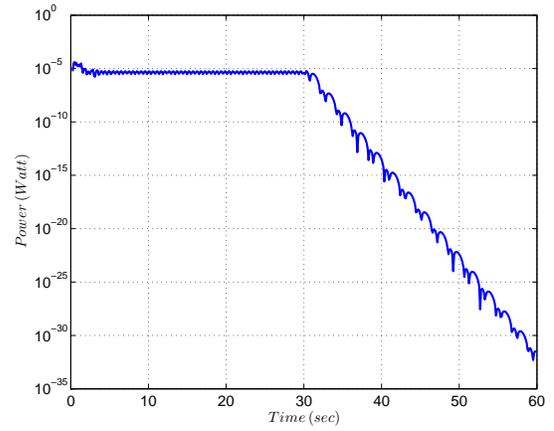
Figure 15: Harvested power at various frequencies: (a) $\omega_P = 0.01\,\mathrm{rad}/sec$; (b) $\omega_P = 0.1\,\mathrm{rad}/sec$; (c) $\omega_P = 1\,\mathrm{rad}/sec$; (d) $\omega_P = 10\,\mathrm{rad}/sec$

Appendix A. Coefficients of the closed-form solution

The coefficients used in the analytical solution presented in Section 6 are as follows

$$b_1 := \frac{a_2\, a_6}{a_1} + a_7, \qquad\qquad b_2 := \frac{a_3\, a_6}{a_1} + a_8,$$

$$c_1 := a_{13} + \frac{a_3\, a_{11}}{a_1}, \qquad\qquad c_2 := a_8 + \frac{a_3\, a_6}{a_1},$$

$$c_3 := a_{10} + \frac{a_5\, a_9}{a_4}, \qquad\qquad c_4 := \frac{a_9}{a_4} - \frac{a_{11}}{a_1} + \frac{a_6\, c_1}{a_1\, c_2},$$

$$b_3 := -\frac{c_4}{c_3}, \qquad\qquad b_4 := \frac{c_1}{c_2\, c_3},$$

$$b_5 := a_{12} - \frac{b_1\, c_1}{c_2} + \frac{a_2\, a_{11}}{a_1}, \qquad\qquad b_6 := \frac{a_{11}}{a_1} - \frac{a_6\, c_1}{a_1\, c_2},$$

$$b_7 := \frac{c_1}{c_2}, \qquad\qquad b_8 := \frac{1}{2}\left(\frac{a_{14} a_6}{a_1} + a_{16} \right),$$

$$b_9 := \frac{a_{17}}{2} + \frac{b_8\, c_1}{c_2} - \frac{a_{11}\, a_{14}}{2\, a_1}, \qquad\qquad k := \sqrt{\frac{b_5}{c_3}},$$

$$c_5 := \frac{1}{2}\left(a_{20} + \frac{a_3\, a_{18}}{a_1} \right), \qquad\qquad c_6 := \frac{b_8\, c_5}{c_2} - \frac{a_{21}}{4} - \frac{a_{14}\, a_{18}}{4\, a_1},$$

$$k_1 := \sqrt{\frac{a_{24}}{c_6}}, \qquad\qquad c_7 := \frac{a_{19}}{2} - \frac{c_5\, b_1}{b_2} + \frac{a_2\, a_{18}}{2\, a_1},$$

$$c_8 := \frac{a_{21}}{4} - \frac{b_8\, c_5}{b_2} + \frac{a_{14}\, a_{18}}{4\, a_1}, \qquad\qquad c_9 := \frac{a_{18}}{2\, a_1} - \frac{a_6\, c_5}{a_1\, b_2},$$

$$m_1 := \frac{c_7 - a_{23}}{c_8}, \qquad\qquad m_2 := \bar{Q}^m\, \frac{c_9}{c_8} + \bar{Q}^e\, \frac{c_5}{b_2\, c_8} - \beta\big|_{x=l}\, \frac{c_7}{c_8},$$

$$m_3 := -\frac{a_{22}}{c_8}.$$

Acknowledgments

References

[1] A. Erturk, D. J. Inman, Piezoelectric Energy Harvesting, first ed., John Wiley & Sons Inc., Chichester, England, 2011.

[2] X. D. Zhang, C. T. Sun, Formulation of an adaptive sandwich beam, Smart Materials and Structures 5 (1996) 814.

[3] A. Benjeddou, M. A. Trinidade, R. Ohayon, A unified beam finite element model for extension and shear piezoelectric actuation mechanisms, Intelligent Material Systems and Structures 8 (1997) 1012–1025.

[4] O. J. Aldraihem, A. A. Khdeir, Smart beams with extension and thickness-shear piezoelectric actuators, Smart Materials and Structures 9 (2000) 1–9.

[5] A. Erturk, Electromechanical Modeling of Piezoelectric Energy Harvesters, Ph.D. thesis, Virginia Polytechnic Institute and State University, 2009.

[6] N. E. duToit, B. L. Wardle, S. G. Kim, Design considerations for MEMS-scale piezoelectric mechanical vibration energy harvesters, Integrated Ferroelectrics 16 (2005) 121–160.

[7] U. Kushnir, O. Rabinovitch, Nonlinear ferro-electro-elastic beam theory, International Journal of Solids and Structures 46 (2009) 2397–2406.

[8] M. Trindade, A. Benjeddou, R. Ohayon, Finite element modelling of hybrid activepassive vibration damping of multilayer piezoelectric sandwich beamspart I: Formulation, International Journal for Numerical Methods in Engineering 51 (2001) 835–854.

[9] M. Trindade, A. Benjeddou, R. Ohayon, Finite element modelling of hybrid activepassive vibration damping of multilayer piezoelectric sandwich beamspart II: System analysis, International Journal for Numerical Methods in Engineering 51 (2001) 855–864.

[10] A. Abdelkefi, F. Najar, N. A. H., S. B. Ayed, An energy harvester using piezoelectric cantilever beams undergoing coupled bending-torsion vibrations, Smart Materials and Structures 20 (2011) 115007.

[11] S. Adhikari, M. Friswell, D. J. Inman, Piezoelectric energy harvesting from broadband random vibrations, Smart materials and Structures 18 (2009).

[12] S. Roundy, P. K. Wright, A piezoelectric vibration based generator for wireless electronics, Smart Materials and Structures 13 (2004) 1131–1142.

[13] A. Tabesh, L. G. Fréchette, An improved small-deflection electromechanical model for piezoelectric bending beam actuators and energy harvesters, Journal of Micromechanics and Microengineering 18 (2008) 104009.

[14] A. Erturk, D. J. Inman, Issues in mathematical modeling of piezoelectric energy harvesters, Smart Materials and Structures 17 (2008) 065016.

[15] S. L. Kok, N. M. White, N. R. Harris, Fabrication and characterization of free-standing thick-film piezoelectric cantilevers for energy harvesting, Measurement in Science and Technology 20 (2009) 124010.

[16] R. Poya, Higher Order Finite Elements for Energy Harvesting Piezoelectric Beams, Master's thesis, Swansea University, Swansea, UK, 2013.

[17] A. S. Henry, G. Park, J. I. Daniel, Estimation of electric charge output for piezoelectric energy harvesting, Strain 40 (2004) 49–58.

[18] D. H. Pearce, A. Hooley, T. W. Button, On piezoelectric super-helix actuators, Sensors and Actuators A: Physical 100 (2002) 281–286.

[19] A. Butz, S. Klinkel, W. Wagner, A geometrically and materially non-linear piezoelectric three-dimensional-beam finite element formulation including warping effects, International Journal for Numerical Methods in Engineering 76 (2008) 601–635.

[20] S. Klinkel, W. Wagner, A piezoelectric solid shell element based on a mixed variational formulation for geometrically linear and nonlinear applications, Computers and Structures 86 (2007) 38–46.

[21] S. Klinkel, D. Legner, W. Wagner, Advanced finite element formulations for modeling thin piezoelectric structures, PAMM: Proceedings in Applied Mathematics and Mechanics 11 (2011) 31–34.

[22] M. Ganapathi, B. P. Patel, M. Touratier, Refined finite element for piezoelectric laminated composite beams, Smart Materials and Structures 13 (2004) N57.

[23] Y. Koutsawa, G. Gaetano, S. Belouettar, Hierarchical FEM modelling of piezo-electric beam structures, Composite Structures 95 (2013) 705–718.

[24] K. D. Hjelmstad, Fundamentals of Structural Mechanics, International series in civil engineering and engineering mechanics. Springer Inc., New York, 2005.

[25] T. J. R. Hughes, The Finite Element Method: Linear Static and Dynamic Finite Element Analysis, Prentice Hall Inc., Englewood Cliffs, New Jersey, 1987.

[26] M. Suri, Analytical and computational assessment of locking in the hp finite element method, Computer Methods in Applied Mechanics and Engineering 133 (1996) 347–371.

[27] L. Chilton, M. Suri, On the selection of a locking-free hp element for elasticity problems, International Journal for Numerical Methods in Engineering 40 (1997) 2045–2062.

[28] A. J. Gil, P. Ledger, A coupled hp-finite element scheme for the solution of two-dimensional electrostrictive materials, International Journal for Numerical Methods in Engineering 91 (2012) 1158–1183.

[29] D. Jin, P. Ledger, A. J. Gil, An hp-fem framework for the simulation of electrostrictive and magnetostrictive materials, Computers and Structures 133 (2014) 131–148.

[30] J. Curiel Sosa, A. J. Gil, Analysis of a continuum-based beam element in the framework of explicit-FEM, Finite Elements in Analysis and Design 45 (2009) 583 – 591.

[31] J. Yang, Special Topics in the Theory of Piezoelectricity, Springer Inc., Dordrecht, Heidelberg, London, New York, 2009.

[32] L. Demkowicz, Computing with hp-Adaptive Finite Elements: Volume 1: One and Two Dimensional Elliptic and Maxwell Problems, Chapman and Hall, Boca Raton FL, USA, 2007.

[33] B. Szabó, I. Babuška, Finite Element Analysis, John Wiley and Sons Inc., New York, 1991.

[34] G. E. Karniadakis, S. J. Sherwin, Spectral/hp Element Methods for CFD, Oxford University Press, Oxford, England, 1999.

[35] R. Poya, FEAPB: Finite Element Analysis of Piezoelectric Beams, https://github.com/romeric/FEAPB, 2013.

[36] B. P. Baillargeon, S. S. Vel, Active Vibration Suppression of Sandwich Beams using Piezoelectric Shear Actuators: Experiments and Numerical Simulations, Smart Materials and Structures 16 (2005) 517–530.

[37] J. N. Reddy, An Introduction to the Finite Element Method, third ed., McGraw-Hill, New York, 2006.